

Post-doctoral: Simulation and measurement of road surface
optical properties

Ruqin Xiao

This work is under **REFLECTIVITY** project

Abstract

Abstract—

Key words—

Contents

1	Introduction	4
1.1	Context and objectives	4
1.2	Mission	5
1.3	Report organization	6
2	Optical properties of road surface	7
2.1	Basic concepts	7
2.1.1	Radiometric quantities	7
2.1.2	Spectral radiometry	8
2.2	Spectral BRDF	9
2.2.1	Properties	12
2.2.2	Isotropic and anisotropic	13
2.3	Solar albedo	14
2.3.1	Types of albedo	14
2.3.2	The link between BRDF and solar albedo	15
3	BRDF models used in road surface	16
3.1	Microfacet-based BRDF models	17
3.1.1	Oren-Nayar BRDF	18
3.1.2	Torrance-Sparrow / Cook Torrance BRDF	20
3.2	Ashikhmin-Shirley BRDF	24
3.3	Simonot BRDF	25

3.4	Kelemen-Kalos BRDF	26
3.5	Burley-Disney BRDF	28
3.6	Lafortune BRDF	29
3.7	Retro-phong BRDF	30
3.8	Hapke's SHOE BRDF model	31
4	Reflectance Measurements of Road Materials	33
4.1	BRDF Measurements of Road Materials	33
4.1.1	BRDF Measurement Set-up	34
4.1.2	Former work on BRDF Measurement of Different Road Materials	34
4.2	Solar Albedo Measurements of Road Materials	45
4.2.1	Albedo Measurement set-up	45
4.2.2	Previous Work on Solar Albedo Measurements of Road Materials	49
5	Spectral BRDF Measurement of road samples	53
5.1	Road samples	54
5.1.1	4 Formulations	54
5.1.2	Construction of single-material samples	55
5.2	Spectral BRDF Measurement	57
5.2.1	Spectral BRDF Measurement set-up: the Gonioreflectometer at Cerema . . .	58
5.2.2	Measurement steps	60
5.2.3	Comparison with UGE	62
5.2.4	Validation with Spectralon	62
5.3	Results	62
5.3.1	Methodology	62
5.3.2	Results of 4 Mixed Road-Material Samples	63
5.3.3	Results of 3 Mastics	63
5.3.4	Results of Single Road-Material Samples	64
5.3.4.1	Lazard	64
5.3.4.2	Garonne	65

5.3.4.3	Gouraudière	65
6	Modelling of road samples	66
6.1	Modelling of Single Road-Material Samples and Mastics	66
6.1.1	Methodology	66
6.1.2	BRDF Fitting to Measurements	67
6.1.2.1	BRDF Fitting: Lazard	67
6.1.2.2	BRDF Fitting: Garonne	67
6.1.2.3	BRDF Fitting: Gouraudière	67
6.1.2.4	Fitting Results of 3 Mastics	67
6.2	Modelling of 4 Mixed Road-Material Samples	67
6.2.1	Existing methods of Mixing BRDF	67
6.2.2	BRDF Construction of F1	67
6.2.3	BRDF Construction of F2	67
6.2.4	BRDF Construction of F3	67
6.2.5	BRDF Construction of F4	67
7	Conclusion and Perspectives	68
7.1	Conclusion	68
7.2	Perspectives	68

Chapter 1

Introduction

1.1 Context and objectives

In our daily lives, we have seen a variety of road surfaces, including bituminous (or asphalt) roads, concrete roads, earthen roads, gravel roads, and murram roads. Among these, bituminous roads are the most commonly seen in our daily transportation due to their practicality, wear resistance and robustness. In the design and operation of mobility systems, many challenges, e.g. climate imperatives, the rise of active modes of transport, and the arrival of autonomous vehicles, require us to rethink a number of practices. In this context, the optical properties of road surface play a fundamental role in optimizing the energy consumption of public lighting installations [1], reduce light pollution [2], control urban temperature [3], and consider perception of road markings [4]. In favor of these issues, it becomes necessary to know the optical properties of road surface or be able to anticipate them when creating a surfacing or predicting their evolution over time. Consequently, this requires conducting a significant number of simulations or measurements.

When discussing optical properties of road surface, both the Bidirectional Reflectance Distribution Function (BRDF) and solar albedo are essential because they provide complementary information about how the surface interacts with light. The former provides detailed directional information, describing the angular distribution of reflected light based on the angle of incoming light and the viewing angle [5]. It captures how surface roughness, texture, and material composition affect

light reflection, affecting the visibility of the road and markings [6]. The latter gives an overall measure of reflected energy, representing the total fraction of incoming solar energy reflected by the road surface, without regard to direction [7]. Road surface with higher solar albedo reduces heat absorption by reflecting more sunlight back into the atmosphere, lowering cooling demands in nearby buildings and contributing to mitigate the damage on road materials.

These two properties depend on the physical characteristics of the road surface, such as roughness and refractive index. However, the measurement of BRDF or solar albedo is costly, not only in terms of instrumentation but also in the time required to measure it. This raises the question: if we already know the physical characteristics of a road surface, is it possible to derive its BRDF and solar albedo without direct measurement? Specifically, if we have a road sample and know its formulation in terms of the material composition, sizes, and proportions. Can we establish a reliable relationship between these parameters and the resulting optical properties? However, the challenge lies in the fact that the relationship between the formulation of a road surface and its corresponding characteristics is not explicitly defined, complicating numerical simulation of the BRDF and so solar albedo. Roads are typically composed of various materials, such as bitumen, different types of aggregates, and fillers, which further adds to the complexity.

To simplify the problem, we propose to focus firstly on several single-component road samples to investigate appropriate BRDF models that can accurately fit their measured results. So the problem becomes how to combine these BRDF models for each single-component to fit the measured BRDF of multi-component road sample. To explore and develop such methods is the objective of this work.

1.2 Mission

To achieve the objective, the mission follows 5 steps:

1. Build several single-component road samples and measure their BRDF;
2. Fit the measured BRDF of each single-component road sample using existing BRDF models;
3. Build several multi-component road samples and measure their BRDF;

4. Explore and develop the method to combine the BRDFs of each single-component to fit the measurement of multi-component road samples;
5. Estimate the solar albedo using BRDF.

1.3 Report organization

This report is structured into the following chapters:

Chapter 2

Optical properties of road surface

2.1 Basic concepts

To provide a clear understanding of the optical properties of road surface, the fundamental terminologies are introduced in this section.

2.1.1 Radiometric quantities

Radiometric quantities provide a way to measure and describe the behavior of radiant energy in terms of light interaction with road surface. They include flux, radiant intensity, irradiance and radiance.

Flux F , is the most fundamental quantity in radiometry [5]. It is also called radiant power, which measures the amount of light that hits a surface over a finite area from all directions per unit time. For a given amount of radiated energy Q at a time duration t , the flux F is expressed as:

$$F(t) = \frac{dQ}{dt} \quad (2.1)$$

As Q is expressed in Joules (J), the unit of F is watts ($W = J \cdot s^{-1}$)

Radiant intensity I , is a correlated measure of flux. It represents the intensity of flux per unit solid angle which is propagate towards some specific direction (θ, φ) toward the the infinitesimal

solid angle $d\vec{\omega}$ [8]. Thus, it can be expressed in terms of flux:

$$I(t, \theta, \varphi) = \frac{dF(t)}{d\vec{\omega}} = \frac{dF(t)}{\sin \theta d\theta d\varphi} \quad (2.2)$$

Notice that the unit of solid angle is the steradian [sr], so the unit of radiant intensity is [$W \cdot sr^{-1}$].

Irradiance E , is another correlated measure of flux in terms of surface area. Different from radiant intensity, it captures the integration over the entire hemisphere Ω of the incident light arriving at a unit surface $ds(p)$ centered on the point p . Essentially, it measures the amount of radiated energy strike a unit area per unit time:

$$E(p, t) = \frac{dF(t)}{ds(p)} \quad (2.3)$$

Its unit is [$W \cdot m^{-2}$]

Radiance L , measures the amount of incident light arriving at a unit surface $ds(p)$ centered on p from a unit solid angle $d\vec{\omega}$ per unit time t . It can be considered as a correlated measure of radiant intensity per unit area or irradiance per unit solid angle:

$$L(p, t, \theta, \varphi) = \frac{d^2F(t)}{|d\vec{\omega} \cdot \vec{n}| d\vec{\omega} ds(p)} = \frac{dI(t, \theta, \varphi)}{\cos \theta ds(p)} = \frac{dE(p, t)}{\sin \theta d\theta d\varphi} \quad (2.4)$$

The product term $\cos \theta ds(p)$ represents the projection of the unit surface $ds(p)$ onto the direction $\vec{\omega}$. According to its definition, the unit of $L(p, t, \theta, \varphi)$ is [$W \cdot m^{-2} \cdot sr^{-1}$].

2.1.2 Spectral radiometry

In the previous section, the definitions of radiometric quantities are given without considering the wavelength. In order to describe the spectral distribution of a radiation, the spectral radiometric quantities are introduced, including spectral flux, spectral intensity, spectral irradiance and spectral radiance.

Spectral flux F_λ , is defined as the flux per unit wavelength and expressed in [$W \cdot nm^{-1}$]:

$$F_\lambda(t) = \frac{dF(t)}{d\lambda} \quad (2.5)$$

Spectral intensity I_λ , is the radiant intensity per unit wavelength and expressed in [$W \cdot sr^{-1} \cdot nm^{-1}$]:

$$I_\lambda(t, \theta, \varphi) = \frac{dI(t, \theta, \varphi)}{d\lambda} \quad (2.6)$$

Spectral irradiance E_λ , is irradiance per unit wavelength and expressed in [$W \cdot m^{-2} \cdot nm^{-1}$]:

$$E_\lambda(p, t) = \frac{E(p, t)}{d\lambda} \quad (2.7)$$

Spectral radiance L_λ , is defined as the radiance per unit wavelength and expressed in [$W \cdot m^{-2} \cdot sr^{-1} \cdot nm^{-1}$]:

$$L_\lambda(p, t, \theta, \varphi) = \frac{dL(p, t, \theta, \varphi)}{d\lambda} \quad (2.8)$$

The measurement of spectral quantities are conducted with instruments such as spectrophotometers which analyze the radiation in adjacent and narrow spectral bands [8]. When analyzing radiation over a broader wavelength range $[\lambda_1, \lambda_2]$, the total measured flux can be calculated by integrating the spectral flux density across the specified waveband. This process accounts for the contribution of all individual wavelengths within the range, providing a cumulative representation of the flux. The computation is expressed as:

$$F(\lambda_1, \lambda_2) = \int_{\lambda_1}^{\lambda_2} F_\lambda d\lambda \quad (2.9)$$

2.2 Spectral BRDF

The BRDF is first introduced by Fred Nicodemus in 1965 [9], which is rigorously defined as the ratio of reflected radiance in a given viewing direction to the incident irradiance from a specified light source direction, at a given surface point p . It is typically expressed in units of sr^{-1} . However, the BRDF alone does not capture the full complexity of how surfaces reflect light across different wavelengths. To gain a more comprehensive understanding of these interactions, we turn to the spectral BRDF which is an extension of the traditional BRDF [8]. It provides a wavelength-dependent function that characterizes how surfaces reflect light at specific incident and reflected angles at a given surface point p , across a narrow spectral bandwidth $\Delta\lambda$. Mathematically, it is expressed as:

$$f_r(p, \lambda, \theta_i, \varphi_i, \theta_r, \varphi_r) = \frac{dL(p, \lambda, \theta_r, \varphi_r)}{dE(p, \lambda, \theta_i, \varphi_i)}, \quad (2.10)$$

where:

- λ is the wavelength of light source;

- θ_i and φ_i are the zenith and azimuth angle of the unit incident direction $\vec{\omega}_i$:

$$\vec{\omega}_i = (x_i, y_i, z_i) = (\sin \theta_i \cos \varphi_i, \sin \theta_i \sin \varphi_i, \cos \theta_i)$$

- θ_r and φ_r are the zenith and azimuth angle of the unit reflected direction $\vec{\omega}_r$:

$$\vec{\omega}_r = (x_r, y_r, z_r) = (\sin \theta_r \cos \varphi_r, \sin \theta_r \sin \varphi_r, \cos \theta_r)$$

- $dL(p, \lambda, \theta_r, \theta_r)$ is the spectral reflected radiance for waveband $\Delta\lambda$;

$$dL(p, \lambda, \theta_r, \theta_r) = \int_{\Delta\lambda} dL_\lambda(p, \theta_r, \varphi_r) d\lambda$$

- $dE(p, \lambda, \theta_i, \varphi_i)$ is the spectral incident irradiance for waveband $\Delta\lambda$.

$$dE(p, \lambda, \theta_i, \theta_i) = \int_{\Delta\lambda} dE_\lambda(p, \theta_i, \varphi_i) d\lambda$$

Replacing the term $dE(p, \lambda, \theta_i, \varphi_i)$ according to Equation (2.4), it can be defined in terms of incident radiance $L_i(p, \lambda, \theta_i, \varphi_i)$:

$$f_r(p, \lambda, \theta_i, \varphi_i, \theta_r, \varphi_r) = \frac{dL(p, \lambda, \theta_r, \theta_r)}{\cos \theta_i L_i(p, \lambda, \theta_i, \varphi_i) d\theta_i d\varphi_i} \quad (2.11)$$

As both radiance and irradiance take into account the wavelength, the unit of spectral BRDF is still $[sr^{-1}]$.

Ideal diffuse reflection

One of the simplest and most widely used BRDF models is the Lambertian reflector, which is based on the assumption of a perfectly diffuse surface [8]. It has an angle-independent BRDF, proportional to their spectral albedo ρ_d for a given wavelength λ :

$$f_{r(Lambertian)}(p, \lambda, \theta_i, \varphi_i, \theta_r, \varphi_r) = \frac{\rho_d}{\pi} \quad (2.12)$$

Ideal specular reflection

In contrast to diffuse reflection, the perfect specular BRDF describes light incoming a given direction is reflected in a single direction following the law of reflection [10]:

$$f_{r(specular)}(p, \lambda, \theta_i, \varphi_i, \theta_r, \varphi_r) = F_r(\lambda, \theta_i) \frac{\delta(\vec{\omega}_r - \vec{\omega}_r')}{\cos \theta_r}, \quad (2.13)$$

where:

- $\vec{\omega}'_r$ is the mirror direction which is symmetric to the incoming direction $\vec{\omega}_i$:

$$\vec{\omega}'_r = 2(\vec{\omega}_i \cdot \vec{n})\vec{n} - \vec{\omega}_i = 2 \cos \theta_i \vec{n} - \vec{\omega}_i = (-\sin \theta_i \cos \varphi_i, -\sin \theta_i \sin \varphi_i, \cos \theta_i)$$

So we can derive its corresponding zenith and azimuth angle $(\theta'_r, \varphi'_r) = (\theta_i, \varphi_i + \pi)$.

- $\delta(\vec{\omega}_r - \vec{\omega}'_r)$ is the delta dirac function:

$$\delta(\vec{\omega}_r - \vec{\omega}'_r) = \begin{cases} \infty, & \text{if } \vec{\omega}_r = \vec{\omega}'_r \\ 0, & \text{otherwise} \end{cases}$$

Notice that Its integral over all directions equals 1:

$$\int_{\Omega} \delta(\vec{\omega}_r - \vec{\omega}'_r) d\vec{\omega}_r = 1$$

This ensures energy conservation in the reflection process.

- $F_r(\lambda, \theta_i)$ is the Fresnel reflectance of unpolarized light for a given wavelength λ following as:

$$F_r(\lambda, \theta_i) = \frac{1}{2} (r_{\parallel}(\lambda, \theta_i) + r_{\perp}(\lambda, \theta_i)) \quad (2.14)$$

$r_{\parallel}(\lambda, \theta_i)$ and $r_{\perp}(\lambda, \theta_i)$ are the conventional Fresnel coefficient [11] for a given wavelength λ , respectively for parallel and perpendicular polarized light. They are given as below while considering different interfaces:

- At the interface of two dielectric media:

$$r_{\parallel}(\lambda, \theta_i) = \left[\frac{\eta_t \cos \theta_i - \eta_i \cos \theta_t}{\eta_t \cos \theta_i + \eta_i \cos \theta_t} \right]^2$$

$$r_{\perp}(\lambda, \theta_i) = \left[\frac{\eta_i \cos \theta_i - \eta_t \cos \theta_t}{\eta_i \cos \theta_i + \eta_t \cos \theta_t} \right]^2$$

Where η_i, η_t are the refraction indices for the incident and transmitted media for a given wavelength λ . θ_t is the transmitted angle between the normal and transmitted direction:

$$\sin \theta_t = \frac{\eta_i * \sin \theta_i}{\eta_t}$$

- At the boundary between a conductor and a dielectric medium:

$$r_{\parallel}(\lambda, \theta_i) = r_{\perp}(\lambda, \theta_i) \frac{\cos^2 \theta_i (a^2 + b^2) - 2a \cos \theta_i \sin^2 \theta_i + \sin^4 \theta_i}{\cos^2 \theta_i (a^2 + b^2) + 2a \cos \theta_i \sin^2 \theta_i + \sin^4 \theta_i}$$

$$r_{\perp}(\lambda, \theta_i) = \frac{a^2 + b^2 - 2a \cos \theta_i + \cos^2 \theta_i}{a^2 + b^2 + 2a \cos \theta_i + \cos^2 \theta_i}$$

Where:

$$\begin{aligned} 2a^2 &= \sqrt{(\eta^2 - k^2 - \sin^2 \theta_i)^2 + 4\eta^2 k^2} + (\eta^2 - k^2 - \sin^2 \theta_i) \\ 2b^2 &= \sqrt{(\eta^2 - k^2 - \sin^2 \theta_i)^2 + 4\eta^2 k^2} - (\eta^2 - k^2 - \sin^2 \theta_i) \\ a^2 + b^2 &= \sqrt{(\eta^2 - k^2 - \sin^2 \theta_i)^2 + 4\eta^2 k^2} \\ \eta + ik &= \frac{\eta_t + ik_t}{\eta_i + ik_i} \end{aligned}$$

Computing the exact Fresnel term can be highly time-consuming. To mitigate this, Schlick proposed an approximation in 1994 [12], which has become widely adopted in computer graphics [11, 13]. This approximation is following as below when considering different interfaces:

- At the interface between 2 dielectric mediums:

$$F_r(\lambda, \theta_i) = F_0(\lambda) + (1 - F_0(\lambda))(1 - \cos \theta_i)^5 \quad (2.15)$$

The term $F_0(\lambda)$ is the reflection coefficient for light incoming parallel to the normal:

$$F_0(\lambda) = \left(\frac{\eta_i - \eta_t}{\eta_i + \eta_t} \right)^2$$

- At the interface between air/vacuum and a conductor:

$$F(\lambda, \theta_i) = \frac{(\eta_t - 1)^2 + 4\eta_t(1 - \cos \theta_i)^5 + k_t^2}{(\eta_t + 1)^2 + k_t^2} \quad (2.16)$$

where η_t is the index of refraction for the conductor and k_t is the absorption coefficient of the conductor.

Notice that when this approximation is used in a microfacet-based BRDF model for describing specular reflection, the angle θ_i corresponds to the local incident angle θ'_i . In geometry, it is the angle between the half-vector direction between half-vector direction $\vec{\omega}_h = \frac{\vec{\omega}_i + \vec{\omega}_r}{|\vec{\omega}_i + \vec{\omega}_r|}$ and the incident direction $\vec{\omega}_i$.

2.2.1 Properties

Similar to traditional BRDF, a physically plausible spectral BRDF also has the below properties:

- **Energy conservation**

A fundamental principle that must be adhered to by all BRDFs, including spectral BRDFs, is energy conservation. This ensures that the amount of light reflected by a surface does not exceed the amount of light incident upon it. Mathematically, this is often represented as:

$$\int_{\varphi_r=0}^{2\pi} \int_{\theta_r=0}^{\frac{\pi}{2}} f_r(p, \lambda, \theta_i, \varphi_i, \theta_r, \varphi_r) \cos(\theta_r) \sin(\theta_r) d\theta_r d\varphi_r \leq 1$$

- **Reciprocity**

The Helmholtz Reciprocity Rule states that the reflection characteristics should remain unchanged if the directions of light incidence and observation are swapped:

$$f_r(p, \lambda, \theta_i, \varphi_i, \theta_r, \varphi_r) = f_r(p, \lambda, \theta_r, \varphi_r, \theta_i, \varphi_i)$$

It ensures that light behaves consistently in all directions.

- **Non-negative**

The spectral BRDF is always non-negative, ensuring that the reflected radiance is physically meaningful:

$$f_r(p, \lambda, \theta_i, \varphi_i, \theta_r, \varphi_r) \geq 0$$

2.2.2 Isotropic and anisotropic

As spectral BRDF is an extension of traditional BRDF, it can be classified into two categories based on whether they exhibit rotational symmetry or not [10, 14]: isotropic and anisotropic. A material is considered isotropic when its reflectance remains constant for a fixed view and illumination, regardless of the rotation of the material around its normal. Mathematically, it can be expressed in term of the azimuth angle difference between incident direction and reflected direction:

$$f_r(p, \lambda, \theta_i, \varphi_i, \theta_r, \varphi_r) = f_r(p, \lambda, \theta_i, \theta_r, \varphi_r - \varphi_i)$$

In contrast, materials whose reflectance is not constant are considered anisotropic.

2.3 Solar albedo

Another important optical property of road surface, solar albedo (also called solar reflectance) is introduced and discussed in this section.

2.3.1 Types of albedo

Solar albedo of a given surface is defined as the ratio of upward and downward radiation flux [15,16]. This ratio can vary between 0 and 1, where 0 indicates no reflection and 1 signifies complete reflection. Surfaces with higher albedo values reflect more sunlight, leading to cooler temperatures, while those with lower values absorb more radiation, resulting in higher temperatures. As such, it becomes an important factor affecting the temperature of a sunlit surface and that of near-surface ambient air temperature.

There are three primary types of albedo [15] that are commonly discussed, each with distinct implications for environmental and climatic conditions.

1. Black sky albedo

When the surface is illuminated with ideal directional radiation, the surface albedo is called black-sky albedo or directional-hemispherical reflectance:

$$\alpha_{black-sky}(\lambda, \theta_i, \varphi_i) = \frac{\int_0^{\pi/2} \int_0^{2\pi} L_\lambda(\theta_r, \varphi_r) d\theta_r d\varphi_r}{E_\lambda(\theta_i, \varphi_i)} \quad (2.17)$$

Where L_λ is the reflected radiance in the direction $\vec{\omega}_r$, and E_λ is the incident irradiance from the direction $\vec{\omega}_i$.

2. White sky albedo

When the surface is illuminated with ideal diffuse radiation, the surface albedo is called white-sky albedo or bi-hemispherical reflectance:

$$\alpha_{white-sky}(\lambda) = \frac{\int_0^{\pi/2} \int_0^{2\pi} L_\lambda(\theta_r, \varphi_r) d\theta_r d\varphi_r}{E_\lambda} \quad (2.18)$$

Different from the term E_λ in black-sky albedo, here it represents the incident irradiance from all directions into the hemisphere.

3. Blue sky albedo

In fact, the solar albedo we measured is usually under natural daylight illumination, including both directional and diffuse radiation. In this case, the surface albedo is called as blue-sky albedo, which can be approximately expressed as a linear combination of black-sky and white-sky albedo:

$$\alpha_{blue-sky}(\lambda, \theta_i, \varphi_i) \approx (1 - D(\tau, \lambda))\alpha_{black-sky}(\lambda, \theta_i, \varphi_i) + D(\tau, \lambda)\alpha_{white-sky}(\lambda) \quad (2.19)$$

Where $D(\tau, \lambda)$ gives the fraction of the diffuse radiation, varying with the aerosol optical wavelength τ and wavelength λ .

For a given waveband, its corresponding surface albedo can be estimated using the following equation:

$$\alpha(\theta_i, \varphi_i) = \frac{\int_{\lambda_1}^{\lambda_2} E_\lambda(\theta_i, \varphi_i) \alpha_\lambda(\theta_i, \varphi_i) d\lambda}{\int_{\lambda_1}^{\lambda_2} E_\lambda(\theta_i, \varphi_i) d\lambda} \quad (2.20)$$

2.3.2 The link between BRDF and solar albedo

According to the definition of BRDF, black-sky albedo and white sky albedo, we can find the link between them. The black-sky albedo can be derived by integrating BRDF over the viewing hemisphere:

$$\alpha_{black-sky}(\lambda, \theta_i, \varphi_i) = \int_{\varphi_r=0}^{2\pi} \int_{\theta_r=0}^{\frac{\pi}{2}} f_r(\lambda, \theta_i, \varphi_i, \theta_r, \varphi_r) \cos \theta_r \sin \theta_r d\theta_r d\varphi_r \quad (2.21)$$

Similarly, the white-sky albedo can be derived by integrating BRDF over the viewing hemisphere and incident hemisphere:

$$\alpha_{white-sky}(\lambda) = \frac{1}{\pi} \int_{\varphi_i=0}^{2\pi} \int_{\theta_i=0}^{\frac{\pi}{2}} \int_{\varphi_r=0}^{2\pi} \int_{\theta_r=0}^{\frac{\pi}{2}} f_r(\lambda, \theta_i, \varphi_i, \theta_r, \varphi_r) \cos \theta_i \sin \theta_i \cos \theta_r \sin \theta_r d\theta_i d\varphi_i d\theta_r d\varphi_r \quad (2.22)$$

For ideal diffuse reflection, we can conclude that the black-sky albedo and the white-sky albedo are equivalent to the albedo ρ used in Equation 2.12 by computing these two equations.

Chapter 3

BRDF models used in road surface

Reflectance models are typically introduced in order to achieve low-parameter representation of the BRDF measurements acquired from road surfaces [6]. Many road surfaces exhibit non-diffuse characteristics, simplified Lambertian assumptions are insufficient for accurate optical predictions. This is especially true for surfaces that include specular peaks due to polishing or for materials that have retro-reflective properties, such as in tunnel markings or retro-reflective coatings [17]. To address these complexities, this chapter explores a range of reflectance models utilized for characterizing the BRDF of various road materials, such as concrete, sand, aggregates.

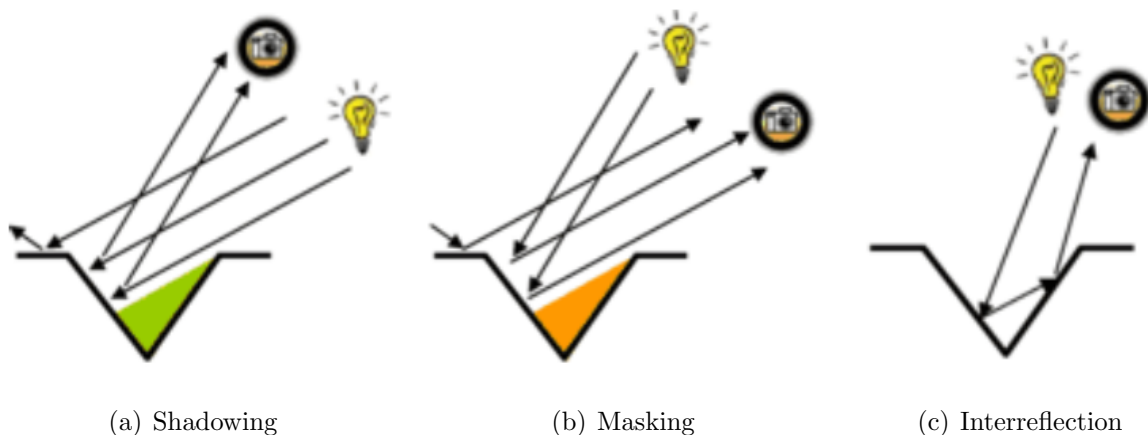


Figure 3.1: Physical phenomena in microfacets

3.1 Microfacet-based BRDF models

This section introduces two widely used reflectance models used in road surface: Oren-Nayar (ON) BRDF for describing diffuse reflection and Torrance Sparrow (TS) / Cook-Torrance (CT) BRDF for describing specular reflection. Both are based on microfacet theory which represents the surface of a collection of small surfaces. In graphics community, microfacet theory was used to derive physically based BRDF [18], and typically accounts for complex geometric and radiometric phenomena:

- shadowing, where the facet is only partially illuminated because the adjacent facet casts a shadow on it, as seen in Fig 3.1(a);
- masking, where the facet is only partially visible to the camera because its adjacent facet occludes it, as seen in Fig 3.1(b).

Their impacts are described using shadowing function and masking function, respectively. A meaningful microfacet model is described by a distribution of normals, which models how the microfacets are statistically oriented, and a microfacet profile, which models how the microfacets are organized on the microfacet. Mathematically, the general microfacet-based BRDF expression is following as:

$$f_r(\lambda, \theta_i, \varphi_i, \theta_r, \varphi_r) = \frac{1}{\cos(\theta_r)\cos(\theta_i)} \int_0^{\pi/2} \int_0^{2\pi} f_{r(M)}(\lambda, \theta_i, \varphi_i, \theta_r, \varphi_r, \theta_m, \varphi_m) \times (\cos \theta'_r)(\cos \theta'_i) G(\theta_i, \varphi_i, \theta_r, \varphi_r, \theta_m, \varphi_m) D(\theta_m, \varphi_m) d\theta_m d\varphi_m, \quad (3.1)$$

where:

- θ_i, φ_i are the zenith and azimuth angles of the unit incident direction $\vec{\omega}_i$,
- θ_r, φ_r are the zenith and azimuth angles of the unit reflected direction $\vec{\omega}_r$,
- θ_m, φ_m are the zenith and azimuth angles of the unit normal of the microfacet $\vec{\omega}_m$,
- θ'_i is the angle between the incident direction $\vec{\omega}_i$ and the normal of the microfacet $\vec{\omega}_m$,
- θ'_r is the angle between the reflected direction $\vec{\omega}_r$ and the normal of the microfacet $\vec{\omega}_m$,

- $f_{r(M)}(\lambda, \theta_i, \varphi_i, \theta_r, \varphi_r, \theta_m, \varphi_m)$ is the BRDF of each microfacet,
- $D(\theta_m, \varphi_m)$ represents the distribution of the normals of the microfacets;
- $G(\theta_i, \varphi_i, \theta_r, \varphi_r, \theta_m, \varphi_m)$ is geometric attenuation function, combining masking G_1 and shadowing G_2 function. It gives the fraction of microfacets with normal $\vec{\omega}_m$ that are visible along the reflected direction $\vec{\omega}_r$, depending on the microfacet profile (e.g. V-cavity microfacet profile and smith microfacet profile) and the distribution of the microfacet's normal [18]. The masking G_1 and shadowing G_2 function are formalized by the following equations:

$$\begin{aligned}\cos \theta_r &= \int_0^{\pi/2} \int_0^{2\pi} G_1(\theta_r, \varphi_r, \theta_m, \varphi_m) (\cos \theta'_r) D(\theta_m, \varphi_m) d\theta_m d\varphi_m \\ \cos \theta_i &= \int_0^{\pi/2} \int_0^{2\pi} G_2(\theta_i, \varphi_i, \theta_m, \varphi_m) (\cos \theta'_i) D(\theta_m, \varphi_m) d\theta_m d\varphi_m\end{aligned}\quad (3.2)$$

3.1.1 Oren-Nayar BRDF

The Oren-Nayar BRDF is widely used for modelling diffuse reflections from rough surfaces, as it provides a more realistic representation of light behavior compared to simpler Lambertian model [6, 19, 19]. This model was first proposed in 1994 [19] by Oren and Nayar, based on microfacet theory adapting V-cavity microfacet profile. More precisely, the surface is assumed as a collection of long, symmetric v-shaped cavities with equal length, each containing two opposing planar facets. This implies that each V-cavity has the two symmetric normals $\vec{\omega}_m$ and $\vec{\omega}'_m$, leading to the following distribution of normals of each microfacet $D(\theta, \varphi)$:

$$D(\theta, \varphi) = \frac{1}{2} \frac{\delta(\vec{\omega} - \vec{\omega}_m)}{\cos \theta_m} + \frac{1}{2} \frac{\delta(\vec{\omega} - \vec{\omega}'_m)}{\cos \theta'_m}$$

Where θ_m, θ'_m are zenith angles of the normals of the microfacet $\vec{\omega}_m, \vec{\omega}'_m$.

The masking or shadowing term can be derived according to Equation(3.2) considering if there is no or one backfacing normal direction:

$$G_1(\theta_r, \varphi_r, \theta_m, \varphi_m) = \min \left(1, 2 \frac{(\cos \theta_m)(\cos \theta_r)}{(\cos \theta'_r)} \right)$$

$$G_2(\theta_i, \varphi_i, \theta_m, \varphi_m) = \min \left(1, 2 \frac{(\cos \theta_m)(\cos \theta_m)}{(\cos \theta'_i)} \right)$$

Considering both masking and shadowing, the term $G(\theta_i, \varphi_i, \theta_r, \varphi_r, \theta_m, \varphi_m)$ can be derived as:

$$G(\theta_i, \varphi_i, \theta_r, \varphi_r, \theta_m, \varphi_m) = \min \left(1, 2 \frac{(\cos \theta_m)(\cos \theta_r)}{(\cos \theta'_r)}, 2 \frac{(\cos \theta_m)(\cos \theta_m)}{(\cos \theta'_i)} \right) \quad (3.3)$$

The distribution of the normals of all microfacets is described using a spherical gaussian distribution with a mean value of zero and a standard deviation α , which serves as a roughness parameter:

$$D_{gaussian}(\theta_m) = ce^{-\frac{\theta_m^2}{2\alpha^2}}, \quad (3.4)$$

where the normalization constant c is:

$$c = \frac{1}{\int_{\varphi_m=0}^{2\pi} \int_{\theta_m=0}^{\frac{\pi}{2}} e^{-\frac{\theta_m^2}{2\alpha^2}} \sin \theta_m d\theta_m d\varphi_m}$$

Besides, the facets are assumed to exhibit diffuse reflection, implying the BRDF of each microfacet $f_{r(M)}$ is defined as shown in Equation (2.12). By substituting $f_{r(M)}$ from Equation(2.12), G from Equation(3.3) and D from Equation(3.4) into Equation(3.1), the reflectance model is obtained. However, the resulting integral can not be easily evaluated. Therefore, Oren and Nayar provided an approximation by using a identified basis function and conducting a large amounts of numerical simulations to evaluate this integral. The approximated expression of directly reflected part is following as:

$$\begin{aligned} f_r^{dir}(\lambda, \theta_i, \theta_r, \varphi) = & \frac{\rho_d}{\pi} [C_1(\alpha) + C_2(\theta_1, \theta_2, \varphi, \alpha) \cos(\varphi) \tan(\theta_2) \\ & + C_3(\theta_1, \theta_2, \alpha) (1 - |\cos(\varphi)|) \tan(\frac{\theta_1 + \theta_2}{2})] \end{aligned}$$

where:

- ρ_d is the albedo of each facet;
- $\varphi = |\varphi_i - \varphi_r|$ is the relative azimuth angle;
- $\theta_1 = \max(\theta_i, \theta_r)$ is the maximum zenith angle between θ_i and θ_r ;
- $\theta_2 = \min(\theta_i, \theta_r)$ is the minimum zenith angles between θ_i and θ_r ;
- α (in radians) is a parameter for the surface roughness, which is gaussian standard deviation in angles of the microfacets normal

- C_1, C_2, C_3 are constant:

$$C_1(\alpha) = 1 - 0.5 \frac{\alpha^2}{\alpha^2 + 0.33}$$

$$C_2(\theta_1, \theta_2, \varphi, \alpha) = \begin{cases} 0.45 \frac{\alpha^2}{\alpha^2 + 0.09} \sin(\theta_1), & \text{if } \cos(\varphi) \geq 0 \\ 0.45 \frac{\alpha^2}{\alpha^2 + 0.09} \left(\sin(\theta_1) - \left(\frac{2\theta_2}{\pi} \right)^3 \right), & \text{otherwise} \end{cases}$$

$$C_3(\theta_1, \theta_2, \alpha) = 0.125 \left(\frac{\alpha^2}{\alpha^2 + 0.09} \right) \left(\frac{4\theta_1\theta_2}{\pi^2} \right)^2$$

In a V-cavity microfacet, apart from the shadowing and masking effects described in microfacet theory, light rays may also bounce between adjacent facets, as seen in Fig 3.1(c). This phenomenon is referred to as inter-reflections. In the case of Lambertian surfaces, the energy in an incident light diminishes rapidly with each inter-reflection bounce [19]. Accordingly, Oren and Nayar consider only two bounces inter-reflections and neglect the subsequent bounces. Similar to direct illumination component, the multiple inter-reflections part is approximated as:

$$f_r^{ms}(\lambda, \theta_i, \theta_r, \varphi) = 0.17 \frac{\rho_d^2}{\pi} \frac{\alpha^2}{\alpha^2 + 0.13} \left(1 - \frac{4\theta_2^2}{\pi^2} \cos(\varphi) \right)$$

Combining the directly reflected part and the multiple inter-reflections part, the complete expression of the ON BRDF is:

$$f_{r(ON)}(\lambda, \theta_i, \theta_r, \varphi) = f_r^{dir}(\lambda, \theta_i, \theta_r, \varphi) + f_r^{ms}(\lambda, \theta_i, \theta_r, \varphi) \quad (3.5)$$

Notice that this model reduces to Lambertian BRDF when the roughness $\alpha = 0$.

This model has been applied to road materials, such as plaster and white sand in [19], where it provides a good fit with experimental measurements, with the fitting parameters $\rho_d = 0.9, \alpha = 30^\circ$ for the former and $\rho_d = 0.8, \alpha = 35^\circ$ for the latter.

3.1.2 Torrance-Sparrow / Cook Torrance BRDF

The specular reflection model of rough surfaces first introduced by Torrance and Sparrow in 1967 has gained widespread attention [6, 19–22]. This model is also based on microfacet theory, where

each facet is assumed to exhibit specular reflection, corresponding to Equation (2.13). Consequently, the BRDF of each microfacet $f_{r(M)}$ presented in Equation(3.1) can be derived as:

$$\begin{aligned} f_{r(M)}(\lambda, \theta_i, \varphi_i, \theta_r, \varphi_r, \theta_m, \varphi_m) &= \left| \frac{\partial \vec{\omega}_h}{\partial \vec{\omega}_i} \right| \frac{F_r(\lambda, \theta'_i) \delta(\vec{\omega}_m - \vec{\omega}_h)}{|\cos \theta'_i|} \\ &= \frac{F_r(\lambda, \theta'_i) \delta(\vec{\omega}_m - \vec{\omega}_h)}{4 |\cos \theta'_i|^2}, \end{aligned}$$

where $\vec{\omega}_h$ is unit halfway vector, and defined as:

$$\begin{aligned} \vec{\omega}_h &= \frac{\vec{\omega}_i + \vec{\omega}_r}{|\vec{\omega}_i + \vec{\omega}_r|} = (x_h, y_h, z_h) \\ x_h &= \frac{x_i + x_r}{\sqrt{(x_i + x_r)^2 + (y_i + y_r)^2 + (z_i + z_r)^2}} \\ y_h &= \frac{y_i + y_r}{\sqrt{(x_i + x_r)^2 + (y_i + y_r)^2 + (z_i + z_r)^2}} \\ z_h &= \frac{z_i + z_r}{\sqrt{(x_i + x_r)^2 + (y_i + y_r)^2 + (z_i + z_r)^2}} \end{aligned} \quad (3.6)$$

The term $\left| \frac{\partial \vec{\omega}_h}{\partial \vec{\omega}_i} \right|$ is the jacobian of the reflection transformation [18, 23]:

$$\left| \frac{\partial \vec{\omega}_h}{\partial \vec{\omega}_i} \right| = \frac{1}{4 |\vec{\omega}_i \cdot \vec{\omega}_h|} = \frac{1}{4 |\cos \theta'_i|}$$

Putting this $f_{r(M)}$ into Equation(3.1), we can replace the integral by the integrand evaluated at $\vec{\omega}_m = \vec{\omega}_h$ according to the delta dirac function $\delta(\vec{\omega}_m - \vec{\omega}_h)$. Thanks to $\vec{\omega}_r \cdot \vec{\omega}_h = \vec{\omega}_i \cdot \vec{\omega}_h$, we arrive the final expression of TS BRDF:

$$f_{r(TS)}(\theta_i, \varphi_i, \theta_r, \varphi_r) = \frac{F_r(\lambda, \theta'_i) G(\theta_i, \varphi_i, \theta_r, \varphi_r, \theta_h, \varphi_h) D(\theta_h)}{4 \cos \theta_i \cos \theta_r} \quad (3.7)$$

Notice that inter-reflections are not taken into account in this model.

It is known that the geometric attention function G given in Equation (3.1) is dependent of microfacet profile. Two widely used microfacet profiles in this model are introduced: V-cavity and smith.

- **V-cavity microfacet profile**

The original formulation of Torrance-Sparrow (TS) model adapted the former profile [20, 24]. Similar to the microfacet profile used in ON model, it represents the surface as a collection of symmetric V-cavity microfacet, leading to the same G function as Equation (3.3). The

probability distribution of the microfacets normals $D(\theta_h)$ is often described by zero-mean Gaussian distribution function [6, 20], as given in Equation (3.4). Later, Cook and Torrance introduced this reflectance model to computer graphics, replacing the Gaussian function with the Beckmann distribution function [18, 25], which is derived from it:

$$D_{Beckmann}(\theta_h) = \frac{\chi^+(\cos \theta_h)}{\pi \alpha^2 \cos^4(\theta_h)} \exp\left(-\frac{\tan^2(\theta_h)}{\alpha^2}\right) \quad (3.8)$$

Where the step function $\chi^+(\cos \theta_h)$ is the binary discard of backfacing microfacet:

$$\chi^+(\cos \theta_h) = \begin{cases} 1, & \text{if } \cos \theta_h > 0 \\ 0, & \text{else} \end{cases} \quad (3.9)$$

Unlike the Gaussian model, the Beckmann distribution gives the absolute magnitude of reflectance without introducing arbitrary constants. However, it is more computationally expensive.

- **Smith microfacet profile**

Building on Cook-Torrance (CT) reflectance model, the Smith microfacet profile was introduced into it later [18]. This profile represents more realistic surface but is more complicated, as it assumes that the microfacets are not auto-correlated. More precisely, it represents a random set of microfacets instead of a continuous surface, where the heights and normals of the microfacets are independent random variables [18]. A commonly used form of smith joint height-correlated masking-shadowing function is given as:

$$G(\theta_i, \varphi, \theta_r, \phi_r, \theta_h, \varphi_h) = \frac{\chi^+(\cos \theta'_r) \chi^+(\cos \theta'_i)}{1 + \Lambda(\theta_r) + \Lambda(\theta_i)}, \quad (3.10)$$

where $\Lambda(\theta_r)$ and $\Lambda(\theta_i)$ are auxiliary functions, which arise naturally when the derivation of masking and shadowing is conducted in the slope domain. This term depends on the chosen distribution function D . And the local incident angle θ'_i and the local reflected angle θ'_r can be computed via the following equations:

$$\begin{aligned} \cos \theta'_i &= \vec{\omega}_i \cdot \vec{\omega}_h \\ \cos \theta'_r &= \vec{\omega}_r \cdot \vec{\omega}_h \end{aligned} \quad (3.11)$$

To describe the statistical orientation of smith microfacets, two common microfacet distributions are used in Cook-Torrance model: **Beckmann distribution** and **GGX (also known as Trowbridge-Reitz)** distribution. The former one is applicable for a wide of surface conditions from smooth to very rough, and its mathematical expression is given in Equation (3.8). It produces a more sharply peaked distribution near the surface normal and falls off more rapidly for grazing angles. Its associated $\Lambda(\theta_r)$ and $\Lambda(\theta_i)$ are:

$$\begin{aligned}\Lambda(\theta_r) &= \frac{\operatorname{erf}(a)-1}{2} + \frac{1}{2a\sqrt{\pi}} \exp(-a^2) \\ \Lambda(\theta_i) &= \frac{\operatorname{erf}(a')-1}{2} + \frac{1}{2a'\sqrt{\pi}} \exp(-a'^2)\end{aligned}\quad (3.12)$$

Where $a = \frac{1}{\alpha \tan \theta_r}$ and $a' = \frac{1}{\alpha \tan \theta_i}$. A given approximated $\Lambda(\theta_r)$ explained in [18, 23] follows as:

$$\Lambda(\theta_r) \approx \begin{cases} \frac{1-1.259a+0.396a^2}{3.535a+2.181a^2}, & \text{if } a < 1.6 \\ 0, & \text{otherwise} \end{cases} \quad (3.13)$$

The approximation of $\Lambda(\theta_r)$ can be obtained by replacing a with a' .

The latter is designed to have a heavier tail, implying that it decays more slowly at grazing angles. Its mathematical expression is given as:

$$D_{GGX}(\theta_h) = \frac{\chi^+(\cos \theta_h)}{\pi \alpha^2 \cos^4(\theta_h) \left(1 + \frac{\tan^2(\theta_h)}{\alpha^2}\right)^2} \quad (3.14)$$

Its corresponding $\Lambda(\theta_r)$ and $\Lambda(\theta_i)$ follows as:

$$\begin{aligned}\Lambda(\theta_r) &= \frac{-1+\sqrt{1+\frac{1}{a^2}}}{2} \\ \Lambda(\theta_i) &= \frac{-1+\sqrt{1+\frac{1}{a'^2}}}{2}\end{aligned}\quad (3.15)$$

Real-world road surface requires an accurate description of surface reflections which cannot be regarded in the traditional ON model. To address this limitation, this model is extended by a specular part, described by TS reflectance model using same v-cavity microfacet profile and the spherical gaussian distribution [6, 19, 20]. Linearly combining TS BRDF $f_{r(CT)}$ and ON BRDF $f_{r(ON)}$ using weighting factors, the new blended BRDF can be expressed as:

$$f_{r(ON-TS)}(\lambda, \theta_i, \varphi_i, \theta_r, \varphi_r) = k_d f_{r(ON)}(\lambda, \theta_i, \varphi_i, \theta_r, \varphi_r) + k_s f_{r(TS)}(\lambda, \theta_i, \varphi_i, \theta_r, \varphi_r) \quad (3.16)$$

Where the weighting factors k_d and k_s are respectively for diffuse component and the specular component. This mixed model is employed for fitting the measured BRDF of the mixed-material road surfaces [6, 20], achieving a good agreement with measurements.

Another blended BRDF by mixing TS model and Lambertian model (Equation (2.12)) is employed for modelling the road material, such as blue or red concrete [20], exhibiting a good fit with the measured BRDF:

$$f_{r(Lambertian-TS)}(\lambda, \theta_i, \varphi_i, \theta_r, \varphi_r) = k_d f_{r(Lambertian)}(\lambda, \theta_i, \varphi_i, \theta_r, \varphi_r) + k_s f_{r(TS)}(\lambda, \theta_i, \varphi_i, \theta_r, \varphi_r) \quad (3.17)$$

3.2 Ashikhmin-Shirley BRDF

This model is physically based model, and controlled by intuitive parameters [26]:

$$f_{r(AS)}(\lambda, \theta_i, \varphi_i, \theta_r, \varphi_r) = k_d f_{r(AS)}^d(\lambda, \theta_i, \varphi_i, \theta_r, \varphi_r) + k_s f_{r(AS)}^s(\lambda, \theta_i, \varphi_i, \theta_r, \varphi_r) \quad (3.18)$$

Where:

- Diffuse component f_r^d :

$$f_{r(AS)}^d(\lambda, \theta_i, \varphi_i, \theta_r, \varphi_r) = \frac{28\rho_d(1 - k_s F_0)}{23\pi} \left(1 - \left(1 - \frac{\cos \theta_i}{2}\right)^5\right) \left(1 - \left(1 - \frac{\cos \theta_r}{2}\right)^5\right)$$

- Specular component f_r^s :

$$f_{r(AS)}^s(\lambda, \theta_i, \varphi_i, \theta_r, \varphi_r) = \frac{\sqrt{(n_u + 1)(n_v + 1)}(\cos \theta_h)^{n_u \cos^2 \varphi_h + n_v \sin^2 \varphi_h}}{8\pi \max(\cos \theta_i, \cos \theta_r) \cos \theta'_i} F(\lambda, \theta'_i)$$

- k_d, k_s are weighting factors respectively for diffuse and specular reflection,
- ρ_d is the diffuse reflectance of substrate under the specular coating,
- F_0 is the specular reflectance at normal incidence:

$$F_0(\lambda) = \left(\frac{\eta_i - \eta_t}{\eta_i + \eta_t}\right)^2$$

- θ_h is the zenith angle of unit half-vector direction $\vec{\omega}_h$, its corresponding cos is given as below:

$$\cos \theta_h = z_h$$

z_h is given in Equation (3.6).

- φ_h is the azimuth angle of the half-vector direction $\vec{\omega}_h$. Its corresponding cos and sin can be computed as:

$$\begin{aligned}\cos \varphi_h &= \frac{x_h}{\sqrt{1-z_h^2}} \\ \sin \varphi_h &= \frac{y_h}{\sqrt{1-z_h^2}}\end{aligned}$$

x_h, y_h, z_h are given in Equation (3.6).

- θ'_r is the local reflected angle (see in Equation (3.11)), which is the angle between the incident direction $\vec{\omega}_r$ and the half-vector $\vec{\omega}_h$,
- n_u, n_v are two phong-like exponents that control the shape of the specular lobe,
- $F(\lambda, \theta'_i)$ is the Fresnel term from Schlick's approximation, as given in Equation (2.15).

This model:

- Physically based
- No reference result to verify the codes

3.3 Simonot BRDF

This model describes the surfaces as a distribution of microfacet where each facet consists of a flat interface on a Lambertian background [27].

$$f_{r(Simonot)}(\lambda, \theta_i, \varphi_i, \theta_r, \varphi_r) = f_{r(Simonot)}^d(\lambda, \theta_i, \varphi_i, \theta_r, \varphi_r) + f_{r(Simonot)}^s(\lambda, \theta_i, \varphi_i, \theta_r, \varphi_r) \quad (3.19)$$

Where:

- Diffuse component f_r^d :

$$f_{r(Simonot)}^d(\lambda, \theta_i, \varphi_i, \theta_r, \varphi_r) = \frac{\rho_d}{\pi(1 - \rho_d r_{10})} (\eta_0/\eta_1)^2 (1 - R_{01}(\theta_i)) (1 - R_{01}(\theta_r))$$

- Specular component f_r^s :

$$f_{r(Simonot)}^s(\lambda, \theta_i, \varphi_i, \theta_r, \varphi_r) = R_{01}(\theta_i) \frac{\delta(\theta_r - \theta_i) \delta(\varphi_i + \pi - \varphi_r)}{\cos \theta_i \sin \theta_i}$$

- ρ_d is the intrinsic background reflectance factor for a given wavelength λ ,

- η_0, η_1 are the refraction indices of the media 0 and 1 for a given wavelength λ , respectively,
- R_{01} is the reflectance of the interface between media 0 and 1:

$$R_{01}(\theta_0) = \frac{1}{2} \left[\frac{\tan^2(\theta_0 - \theta_1)}{\tan^2(\theta_0 + \theta_1)} + \frac{\sin^2(\theta_0 - \theta_1)}{\sin^2(\theta_0 + \theta_1)} \right]$$

– when $\theta_0 = \theta_i$, $\sin \theta_1 = \frac{\eta_0 \sin \theta_i}{\eta_1}$

– when $\theta_0 = \theta_r$, $\sin \theta_1 = \frac{\eta_0 \sin \theta_r}{\eta_1}$

- r_{10} is the reflectance from medium 1:

$$1 - r_{10} = (\eta_0 / \eta_1)^2 (1 - r_{01})$$

- r_{01} is the reflectance of a flat interface illuminated by Lambertian light from medium 0 is derived from Fresnel's reflectance:

$$r_{01} = \int_0^{\pi/2} R_{01}(\theta_0) \sin 2\theta_0 \theta_0$$

- δ is a dirac delta function:

$$\delta(\theta_r - \theta_i) = \begin{cases} \infty, & \text{if } \theta_r = \theta_i \\ 0, & \text{otherwise} \end{cases}$$

This model:

- Not sure Physically based
- reference result to verify the codes

3.4 Kelemen-Kalos BRDF

This microfacet-based model is physically based model [28]:

$$f_{r(KK)}(\lambda, \theta_i, \varphi_i, \theta_r, \varphi_r) = f_{r(KK)}^{matt}(\lambda, \theta_i, \varphi_i, \theta_r, \varphi_r) + f_{r(KK)}^s(\lambda, \theta_i, \varphi_i, \theta_r, \varphi_r) \quad (3.20)$$

Where:

- Matt component f_r^{matt} accounts for multiple reflections and re-emissions of previously absorbed photons:

$$f_{r(KK)}^{matt}(\lambda, \theta_i, \varphi_i, \theta_r, \varphi_r) = \rho_d \frac{(1 - \rho_s(\theta_i))(1 - \rho_s(\theta_r))}{\pi(1 - \bar{\rho}_s)}$$

- Specular component f_r^s represents single reflections

$$f_{r(KK)}^s(\lambda, \theta_i, \varphi_i, \theta_r, \varphi_r) = \frac{D(\theta_h)F_r(\lambda, \theta'_i)}{4 \cos^2 \theta'_i}$$

- ρ_d is a wavelength dependent diffuse albedo,
- $\rho_s(\theta_i)$ and $\rho_s(\theta_r)$ are the albedos of the specular component:

$$\begin{aligned}\rho_s(\theta_i) &= \int_0^{\pi/2} \int_0^{2\pi} f_{r(KK)}^s(\lambda, \theta_i, \varphi_i, \theta_r, \varphi_r) \cos \theta_r \sin \theta_r d\theta_r d\varphi_r \\ \rho_s(\theta_r) &= \int_0^{\pi/2} \int_0^{2\pi} f_{r(KK)}^s(\lambda, \theta_i, \varphi_i, \theta_r, \varphi_r) \cos \theta_i \sin \theta_i d\theta_i d\varphi_i\end{aligned}$$

- $\bar{\rho}_s$ is the average albedo of specular component:

$$\bar{\rho}_s = \frac{1}{\pi} \int_0^{\pi/2} \int_0^{2\pi} \rho_s(\theta_r) \cos \theta_r \sin \theta_r d\theta_r d\varphi_r$$

- The local including angle θ'_i is the angle between the incident direction $\vec{\omega}_i$ and the half-vector direction $\vec{\omega}_h$. Its corresponding cos and sin can be computed using Equation (3.11).
- $F_r(\lambda, \theta'_i)$ is the Fresnel term as described in Section 2.2 of Chapter 2.
- $D(\theta_h)$ is microfacet orientation probability density function. This model utilized 3 different distribution functions: Beckmann, Ward and Phong. The Beckmann distribution function is given as:

$$D_{Beckmann}(\theta_h) = \frac{1}{\alpha^2 \cos^4 \theta_h} e^{-\left(\frac{\tan^2 \theta_h}{\alpha^2}\right)} \quad (3.21)$$

The Ward distribution function is following as:

$$D_{Ward}(\theta_h) = \frac{1}{\pi \alpha^2 \cos^3 \theta_h} e^{-\left(\frac{\tan^2 \theta_h}{\alpha^2}\right)} \quad (3.22)$$

The Phong distribution function is :

$$D_{Phong}(\theta_h) = \frac{m+1}{2\pi} \cos^m \theta_h \quad (3.23)$$

- α is the surface roughness
- m is the specular reflectivity.

This model:

- Physically based
- reference result to verify the codes

3.5 Burley-Disney BRDF

This model is microfacet based model, but may not physically based [29]:

$$f_{r(BD)}(\lambda, \theta_i, \varphi_i, \theta_r, \varphi_r) = f_{r(BD)}^d(\lambda, \theta_i, \varphi_i, \theta_r, \varphi_r) + f_{r(TS)}^s(\lambda, \theta_i, \varphi_i, \theta_r, \varphi_r) \quad (3.24)$$

- Diffuse component f_r^d :

$$f_{r(BD)}^d(\lambda, \theta_i, \varphi_i, \theta_r, \varphi_r) = \frac{\rho_d}{\pi} (1 + (F_D(\theta'_i) - 1)(1 - \cos \theta_i)^5)(1 + (F_D(\theta'_i) - 1)(1 - \cos \theta_r)^5)$$

- Specular component f_r^s is Torrance-Sparrow BRDF given in Equation (3.7). Notice that the author utilized 3 microfacet distribution functions: Berry, Trowbridge-Reitz (TG, also called GGX) and Generalized Trowbridge-Reitz (TGR):

$$\begin{aligned} D_{Berry}(\theta_h) &= c/(\alpha^2 \cos^2 \theta_h + \sin^2 \theta_h) \\ D_{TR}(\theta_h) &= c/(\alpha^2 \cos^2 \theta_h + \sin^2 \theta_h)^2 \\ D_{GTR}(\theta_h) &= c/(\alpha^2 \cos^2 \theta_h + \sin^2 \theta_h)^\gamma \end{aligned}$$

They use the G term derived for GGX by Wlater [23] and the Fresnel term of Schlick approximation given in Equation (2.15).

- θ'_i is the angle between the incident direction $\vec{\omega}_i$ and the half-vector direction $\vec{\omega}_h$, which is given in Equation (3.11),
- ρ_d is the diffuse albedo,
- $F_D(\theta'_i)$ is:

$$F_D(\theta'_i) = 0.5 + 2\alpha_d \cos^2 \theta'_i$$

- α_d is the surface roughness,
- c is a scaling constant,
- α is roughness parameter from 0 to 1,
- γ is suggested to between 1 and 2.

This model:

- Not physically based
- No reference result to verify the codes

3.6 Lafourture BRDF

A multifunctional empirical reflectance model introduced by Eric Lafourture and his collaborators in 1997 [30, 31], was used to fit measurements from realistic surface. This model is developed based on Phong model [31], decomposed in a sum of lobes, where each lobe represents a specific component of reflection (e.g., specular, diffuse, or retro-reflection):

$$f_{r(1-lobe)}(\theta_i, \varphi_i, \theta_r, \varphi_r) = \rho \max(C_x \overrightarrow{\omega_r} \cdot \overrightarrow{\omega_i} + C_y \overrightarrow{\omega_r} \cdot \overrightarrow{\omega_i} + C_z \overrightarrow{\omega_r} \cdot \overrightarrow{\omega_i})^n, \quad (3.25)$$

where ρ and n are the albedo and the specular reflectivity. The terms C_x, C_y, C_z are diagonal coefficients which can be seen as weighting the terms of the dot product $\overrightarrow{\omega_r} \cdot \overrightarrow{\omega_i}$. It is worth noting that $C_x = C_y$ leading to isotropic directional-diffuse lobe, otherwise anisotropic. The term n represents the specular reflectivity. When $n = 0$ and $n \rightarrow \infty$, this model corresponds to lambertian model and specular model, respectively. To represent a complex realistic reflectance functions, Lafourture computes a sum of several primitive functions presented in the form of Equation (3.25) by absorbing the albedo ρ and the other parameters:

$$f_{r(Lafourture)}(\theta_i, \varphi_i, \theta_r, \varphi_r) = \max \left(\sum_i \rho_i [C_{x,i} \omega_{r_x} \omega_{i_x} + C_{y,i} \omega_{r_y} \omega_{i_y} + C_{z,i} \omega_{r_z} \omega_{i_z}]^{n_i}, 0 \right) \quad (3.26)$$

Where each primitive function i is defined by the parameters $C_{x,i}$ ($= C_{y,i}$), $C_{z,i}$ and n_i . This model allows us to fit the measured BRDF of road surface in different status (e.g. dry and wet [31] using the following fitting parameters), where the materials of roads are not specified:

- dry road: $\rho_d = 0.2, \rho_s = 0.3, C_x = -1, C_y = -1, C_z = 1, n = 5$
- wet road: $\rho_d = 0.2, \rho_s = 0.8, C_x = -1, C_y = -1, C_z = 1, n = 15$

Furthermore, its mathematical formulation renders the model computationally efficient and relatively simple, making it a promising choice for fitting the measured BRDF in this study.

3.7 Retro-phong BRDF

In [32], a new extended Phong model was introduced by Spierings et al. in 2023. The authors took into account the effect of retro-reflection for road markings. In essence, this model is a linear combination of Lambertian reflector and Phong reflector:

$$f_{r(Retro-Phong)}(\theta_i, \phi_i, \theta_r, \phi_r) = \frac{k_d}{\pi} + \frac{k_s(\theta_i)(n+2)}{2\pi} (\vec{\omega}_{is} \cdot \vec{\omega}_r)^n + \frac{k_r(\theta_i)(n+2)}{2\pi} (\vec{\omega}_i \cdot \vec{\omega}_r)^n \quad (3.27)$$

Where k_d , k_s and k_r are the parameters for diffuse component, specular component and retro-reflection component. And $\vec{\omega}_{is}$ is the specular reflection unit vector in the direction of $\varphi_i + \pi$. To satisfy the principle of energy conservation, these three factors are subject to the following constraint:

$$k_d + k_s + k_r < 1$$

Besides, the parameter k_r can be expressed as a simple linear function of the incident angle θ_i :

$$k_r(\theta_i) = k_1(1 - \cos(\theta_i)) + k_2$$

And the parameter k_s can be represented as a simple exponential function:

$$k_s = k_3 e^{k_4(1 - \cos(\theta_i))}$$

This model has been employed for 3 road marking materials [32] containing glass beads, achieving a good fit with the measured results using the following fitting parameters:

- SWARCOLimboplast D480 withMegalux 0.6-1.5 KT14

$$k_d = 0.620, n = 24, k_1 = 0.158, k_2 = 0.0145, k_3 = 0.00133, k_4 = 5.47$$

- SWARCOLimboplast D480 with P21 3:1

$$k_d = 0.594, n = 24, k_1 = 0.0696, k_2 = 0.0733, k_3 = 5.58e - 05, k_4 = 8.74$$

- 3MStamark A650

$$k_d = 0.701, n = 68, k_1 = 0.184, k_2 = 0.153e - 12, k_3 = 0.00570, k_4 = 3.40$$

3.8 Hapke's SHOE BRDF model

A well-known semi-empirical BRDF model widely used for beach sand desert was developed by Hapke in the 1980s [33–35]. This model is based on radiative transfer theory and formally incorporated the Shadow Hiding Opposition Effect (SHOE), and typically expressed as:

$$f_{r(Hapke-SHOE)}(\theta_i, \varphi_i, \theta_r, \varphi_r) = \frac{\rho_{ss}}{4\pi} \frac{1}{\cos \theta_i + \cos \theta_r} \{ [1 + B(g)] p(g) + H(\theta_i)H(\theta_r) - 1 \}, \quad (3.28)$$

where:

- θ_i, φ_i are the incident zenith and azimuth angles.
- θ_r, φ_r are the emitted reflectance zenith and azimuth angles.
- ρ_{ss} is the single scattering albedo.
- g is the phase angle, which is the zenith angle difference between the incident direction and emitted reflectance direction.
- $B(g)$ is the opposition effect term specifically incorporates the SHOE:

$$B(g) = \frac{B_0}{1 + \frac{1}{h \tan(g/2)}}$$

- B_0 is the height of the backscatter peak;
- h is width of the backscatter peak;
- $p(g)$ is the scattering phase function, which quantifies the angular distribution of scattered light relative to the direction of the incoming light.

In general, the scattering behaviors are usually classified into 3 types:

- forward scattering

- backward scattering
- isotropic (light is scattered equally in all direction, indicating $p(\theta) = 1$)

In the Henyey-Greenstein (HG) phase function expressed in the following equation, these behaviors are described by a single parameter ζ (also called asymmetry factor), corresponding to $\zeta > 0$, $\zeta < 0$ and $\zeta = 0$ respectively.

$$p(g) = p_{HG}(g) = \frac{1 - \zeta^2}{(1 + \zeta \cos(g) + \zeta^2)^{3/2}}$$

- $H(\theta)$ is the angular dependent function:

$$H(\theta) = \frac{1 + 2 \cos \theta}{1 + 2 \cos \theta \sqrt{1 - \rho_{ss}}}$$

To fit the measured BRDF, this model is required to find the 4 unknown parameters which are the SHOE backscatter parameters B_0 and h , and the asymmetry factor ζ and the single scattering albedo ρ_{ss} . This complicated parameterization may lead to high computation complexity and so expensive time cost. To address this, some researchers made minor modification by substituting the product $[1 + B(g)] p(g)$ of Hapke's SHOE model with a series expansion of Legendre Polynomials $\left\{1 + \sum_{n=1}^N a_n P_n\right\}$. As such, the final expression of this model becomes:

$$f_{r(Hapke-SHOE)}(\theta_i, \varphi_i, \theta_r, \varphi_r) = \frac{\rho_{ss}}{4\pi} \frac{1}{\cos \theta_i + \cos \theta_r} \left\{ \sum_{n=1}^N a_n P_n + H(\theta_i) H(\theta_r) \right\} \quad (3.29)$$

Where P_n represents the Legendre Polynomials of order n starting from 1, and the coefficients a_n are the parameters fitted to the Measurements data. This modified model is also called as Hapke SPF BRDF model, which does not require the parameters B_0 and h . In [34], this model was shown to exhibit a good fit with the measured data for desert sand (collected from Mountain Pass, California, USA), with incident zenith angles varying from 0° to 70° across the wavelength range of $400 - 2400nm$.

Chapter 4

Reflectance Measurements of Road Materials

Road surfaces are inherently heterogeneous owing to variations in material composition, aging, weathering, and surface texture. These variations cause spatial and temporal changes in reflectance characteristics that influence both the visual performance of lighting installations and the thermal behavior contributing to urban heat island effects. To better understand these changes, numerous field and laboratory optical measurements of road surface materials have been conducted in recent decades, focusing mainly on BRDF [6,19,20,32] and solar albedo [7,16,36,37]. The former quantifies the angular distribution of reflected light, which is critical for optimizing visibility, and the latter represents the fraction of solar reflected radiation which governs pavement thermal performance. This chapter provides the overview of the measurements conducted in the past twenty years in terms of BRDF and solar albedo of different materials of roads.

4.1 BRDF Measurements of Road Materials

In road surface analysis, BRDF measurements offer a detailed understanding of surface reflectance properties, that impacts not only human safety but also the performance of automated systems, such as LiDAR and camera-based sensors in autonomous vehicles.

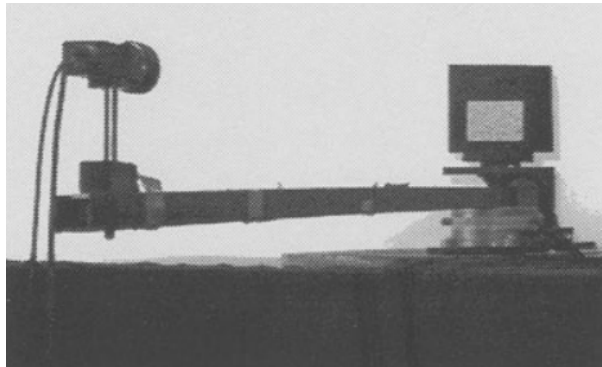
4.1.1 BRDF Measurement Set-up

The BRDF measurement systems for road surface can be broadly categorized into two types: laboratory-based and field-based approaches. The former is typically conducted under controlled environments where factors such as lighting, geometry, and surface conditions can be precisely controlled. The classic laboratory-based systems, such as gonioreflectometer [8, 19, 32] and goni-spectroradiometer if the detection is spectral [20, 34, 35], observe the same surface sample under varying observer and light source position, as seen in Fig 4.1. They are commonly composed of the goniometer used to change the angles of incidence and detection (e.g. by rotating the robot swing arms [8, 19, 34], as seen in Fig 4.1(a) and Fig 4.1(c)), the light source and the detection sensors (e.g. camera, spectroradiometer). In many studies, halogen lamp is used as the light source due to its spectrum close to solar spectrums [8, 20, 32, 34, 35].

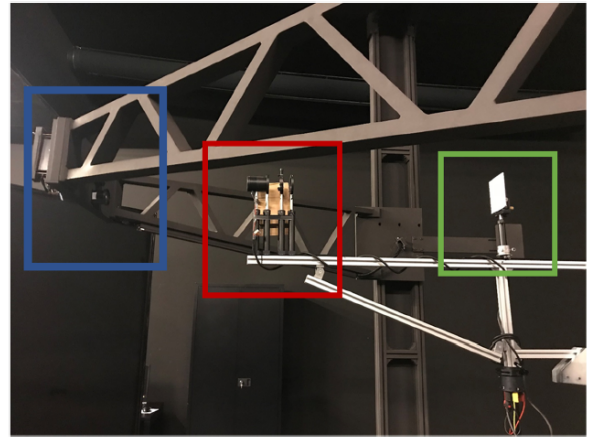
The latter is essential to obtain realistic data of road surface BRDF under actual environmental conditions, such as varying sunlight (from sunrise to sunset), weather (e.g. sunny, cloudy, rainy), and surface states (dry or wet). An example of such a setup is vehicle-based automotive measurement systems [6] (see in Fig 4.2(a)), where natural sunlight serves as the light source and detection sensor, such as camera, is mounted on the car's front window. Apart from this set-up, the lab-based set-up presented in Fig 4.1(c) is extended to measure the soil surface outside [34] by digging a small trench so that the pivot point of the pendulum arm coincided with the soil surface, as shown in Fig 4.2(b)

4.1.2 Former work on BRDF Measurement of Different Road Materials

In practical applications, road surfaces like asphalt and concrete are commonly made from a combination of aggregates and binders. The optical properties of these road materials have been extensively studied to support accurate modeling. To evaluate the accuracy of their diffuse reflectance model developed in 1993 [19], Oren and Nayar conducted several experiments restricted to the visible spectrum, using road-like materials as test samples, such as plaster and white sand. Their experiment set-up is given in Fig 4.1(a), where a 512×480 pixel charged-coupled device



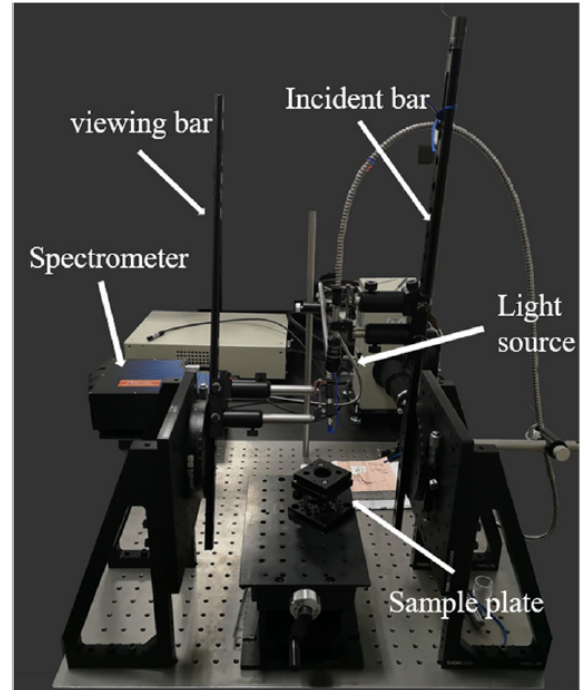
(a) Gonioreflectometer using a long beam



(b) Large near-field gonioreflectometer



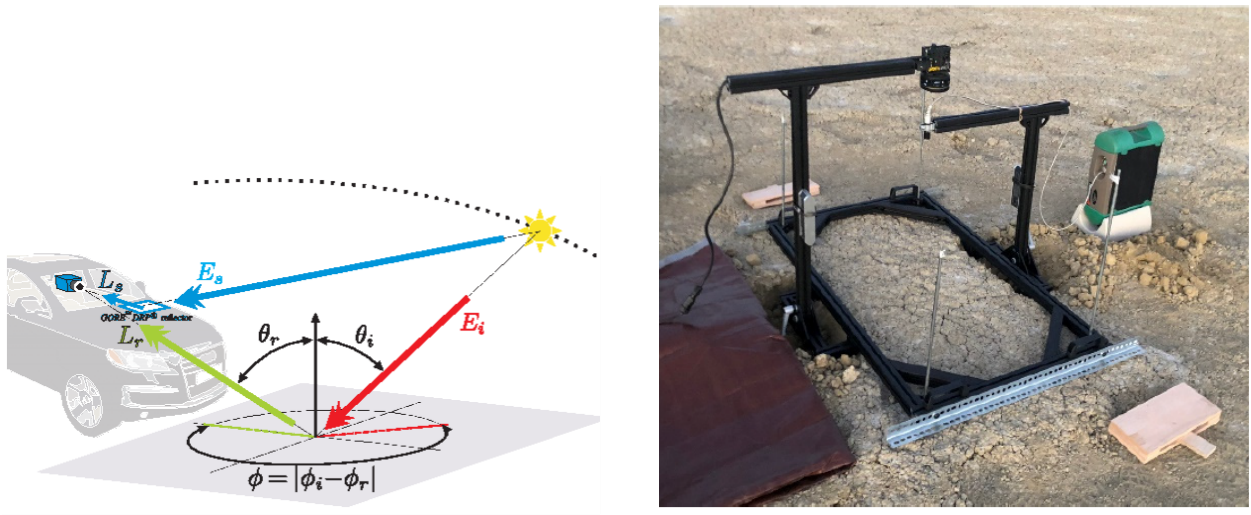
(c) Goni-spectroradiometer using 2 swing arms



(d) Goni-spectroradiometer using two bars

Figure 4.1: BRDF Laboratory measurement set-up

(CCD) camera as receiver is mounted at the end of a 6 foot long beam and 300 Watt incandescent light source is used to illuminate the sample. A pair of fitting parameters of their BRDF model (ON Model as described in Section (3.1.1)), diffuse albedo ρ and surface roughness σ were empirically chosen to obtain the best fit with the measured radiance. The optimal parameter values were found to be $\rho = 0.9$, $\sigma = 30^\circ$ for plaster, and $\rho = 0.8$, $\sigma = 35^\circ$ for white sand, as shown in Fig 4.3 and Fig 4.4 respectively. In both figures, the solid lines and the dotted points respectively show



(a) Vehicle-Mounted set-up

(b) Gonioreflectometer using 2 swing arms

Figure 4.2: BRDF Field-based measurement set-up

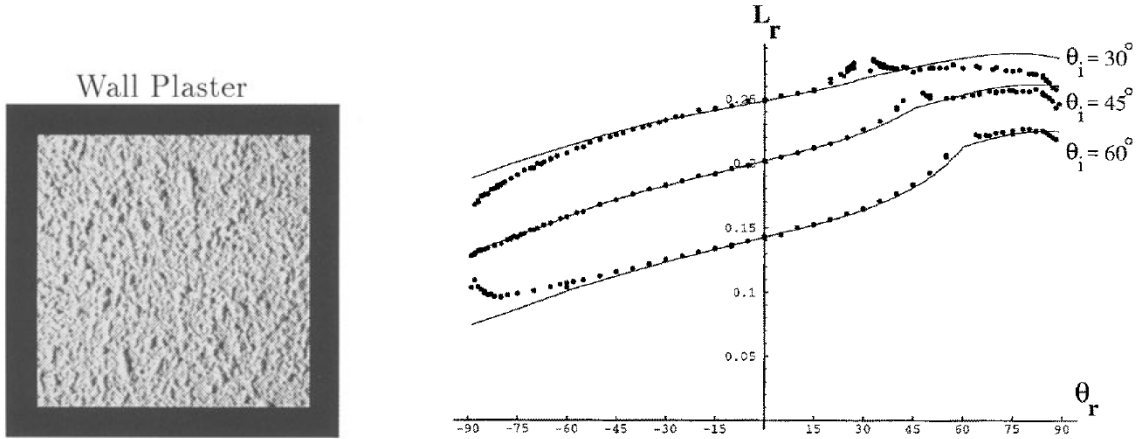


Figure 4.3: Plaster: Oren Nayar model fitting to measured radiance

the radiance predicted by ON model and the measured radiance. Notice that these measurements were made in the plane of incidence ($\varphi_r = \varphi_i$ and $\varphi_r = \varphi_i + \pi$ corresponding to negative and positive values of θ_r). For both plaster and white sand, the measured radiance shows a clear peak in the specular direction, where the this model exhibits poor fitting performance. This indicates that ON model is not well-suited for capturing specular reflectance.

To compensate for this deficiency, Meister extended ON model by linearly combining it with a specular reflectance model (TS model as described in Section (3.1.2)) to fit spectral BRDF measurement for asphalt respectively at 425nm and 660nm over the period from 1995 to 2000 [20], as

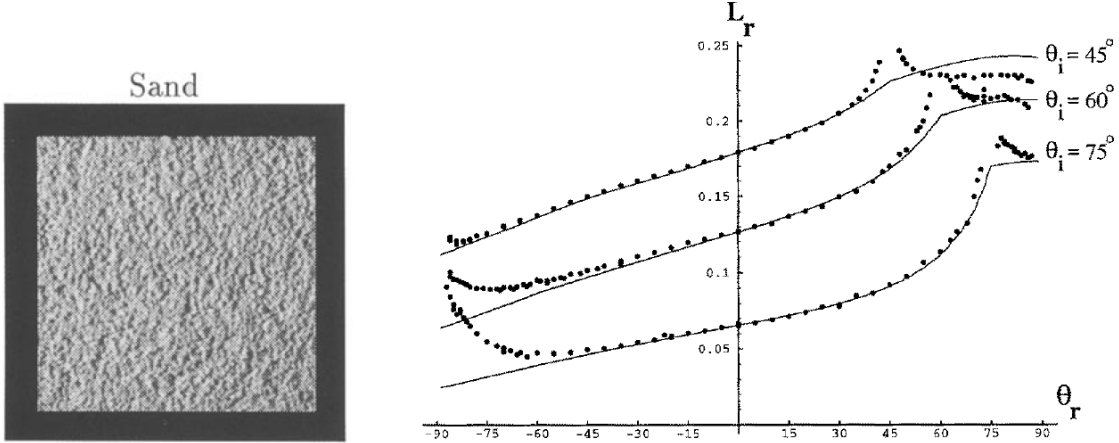


Figure 4.4: White sand: Oren Nayar model fitting to measured radiance

illuminated in Fig 4.5. In addition, he also applied a mixed model which linearly combined Lambertian model and TS model to fit the measured spectral BRDF of blue/red concrete respectively at the same wavelength, as shown in Fig 4.6 and Fig 4.7. These measurements were performed at the European Goniometric Facility (EGO) in Italy using a specially designed goniometer. Instead of employing a rotating robotic arm used by Oren and Nayar, this goniometer is constructed using two quarter arcs with a radius of 2 meters, which allow for the flexible mounting of a sensor and a light source [20]. To measure the spectral BRDF, this setup was modified by replacing the camera with an SE590 spectroradiometer, capable of capturing wavelengths in the range of 400 nm to 1100 nm. A 1000-watt halogen lamp was used as the light source due to its spectral similarity to sunlight. As observed from Fig 4.5 to Fig 4.7, the measured BRDFs were well fitted across most configurations.

In addition to the laboratory-based setup, Roser et al. conducted several experiments directly on natural concrete road surfaces using a three-dimensional geometric model of the automotive BRDF measurement system [6], as shown in Fig 4.2. The camera with known orientation was mounted behind the windshield, and sunlight was serving as the sole source of illumination. This system leverages single grayscale images, integrated with GPS and vehicle heading data, to estimate the reflectance properties of small road patches under both dry and damp conditions. The resulting measured data were subsequently fitted using the extended ON reflectance model that is same as the one used by Meister, as seen in Fig 4.8. This extended model and their parameters were able

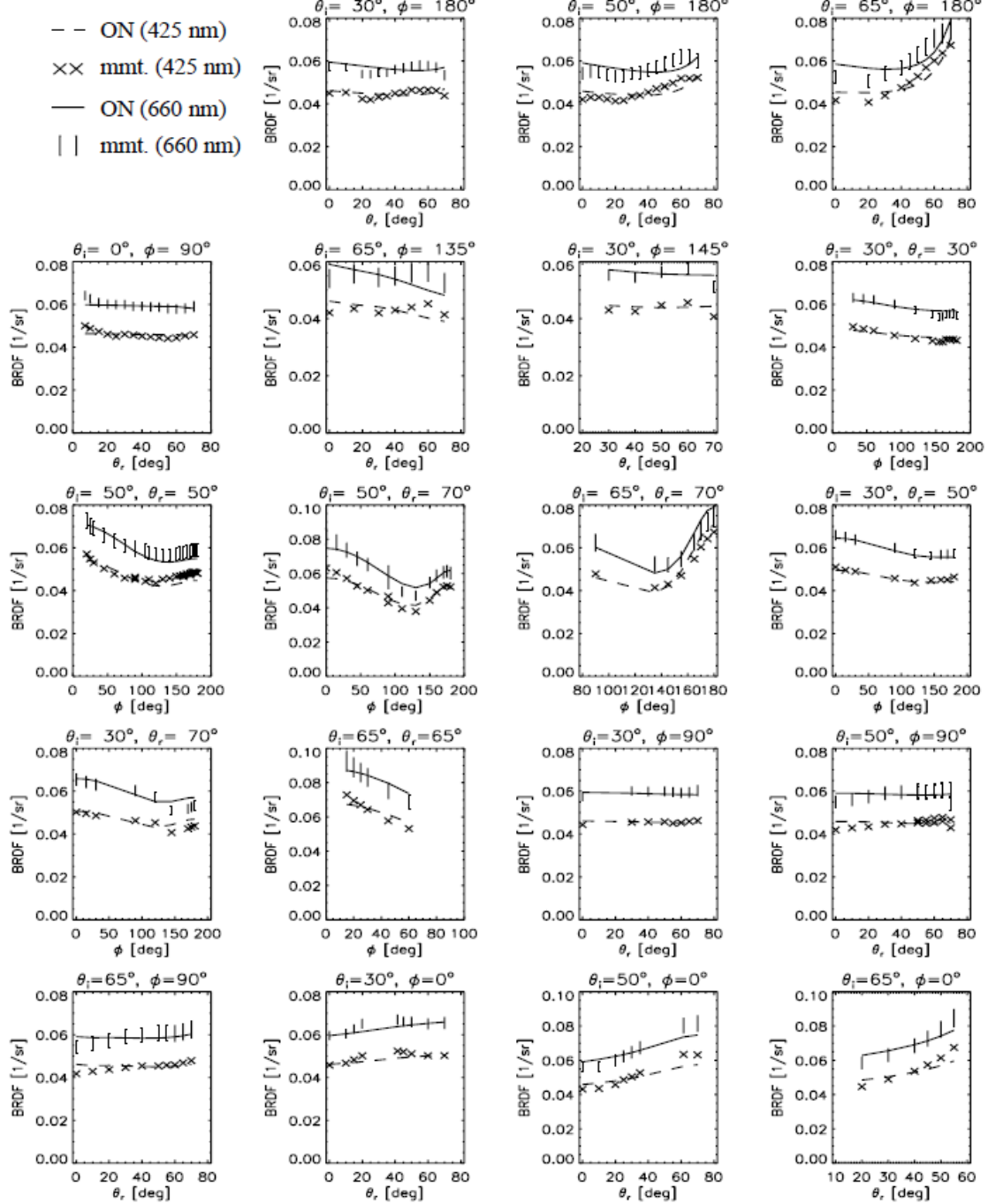


Figure 4.5: Asphalt: mixed reflectance model (ON + CT) fitting to measured BRDF

to successfully differentiate between different pavement reflection conditions.

In recent years, Wise et al. conducted extensive measurements on beach sands under darkened conditions [34], using a goniometer-based setup shown in Fig.4.1(c) that was transitioned to field use as illuminated in Fig 4.2(b). A spectroradiometer covering the $400 - 2400\text{nm}$ range and

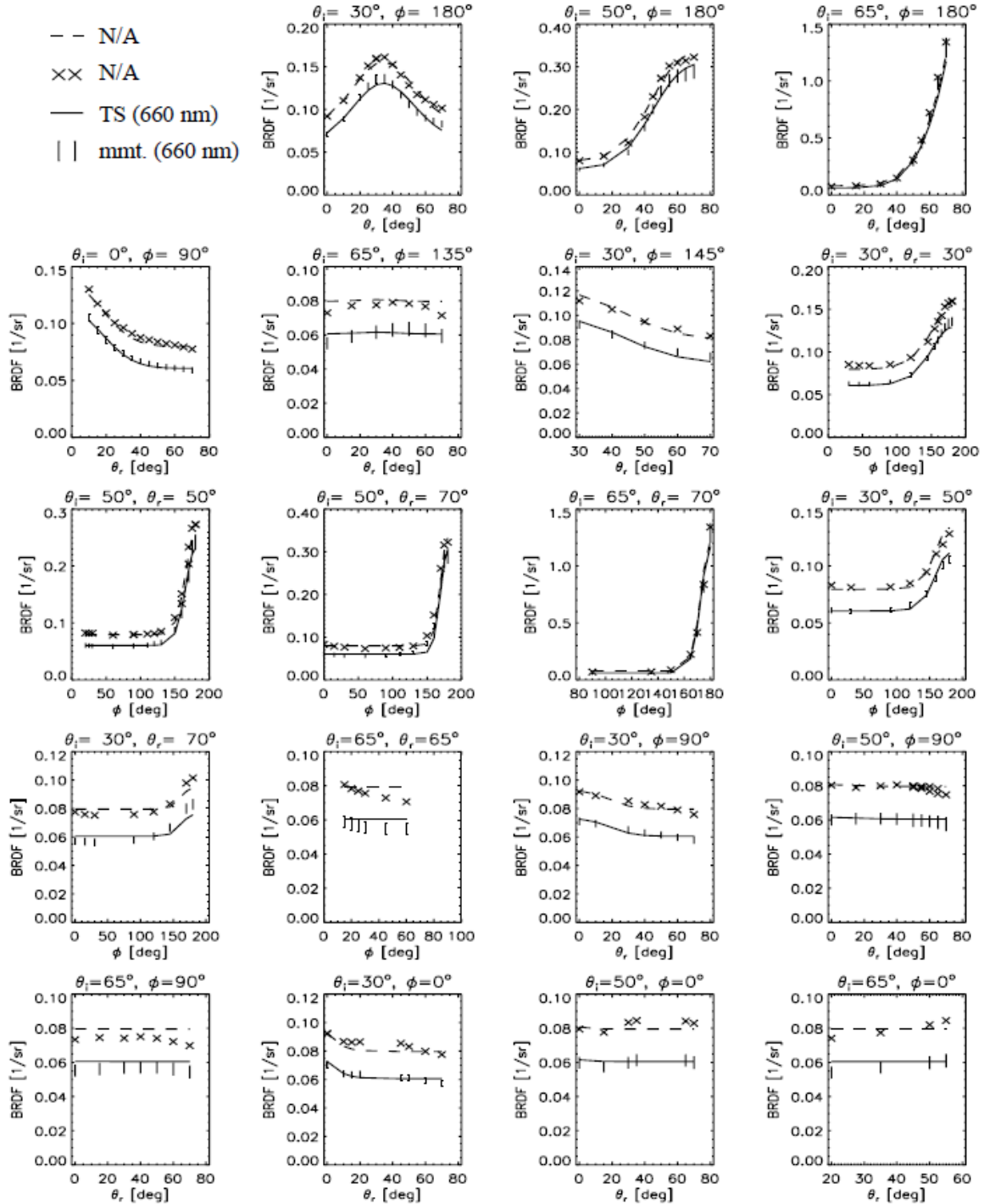


Figure 4.6: Blue concrete: mixed reflectance model (Lambertian + CT) fitting to measured BRDF

a halogen lamp were employed in their experiments, and were mounted on a portable, manually operated goniometer constructed from aluminum struts. In this goniometer design, the platform at the base measured $122 \times 61\text{cm}$ and supported two swing arms, measuring 46cm and 66cm in length,

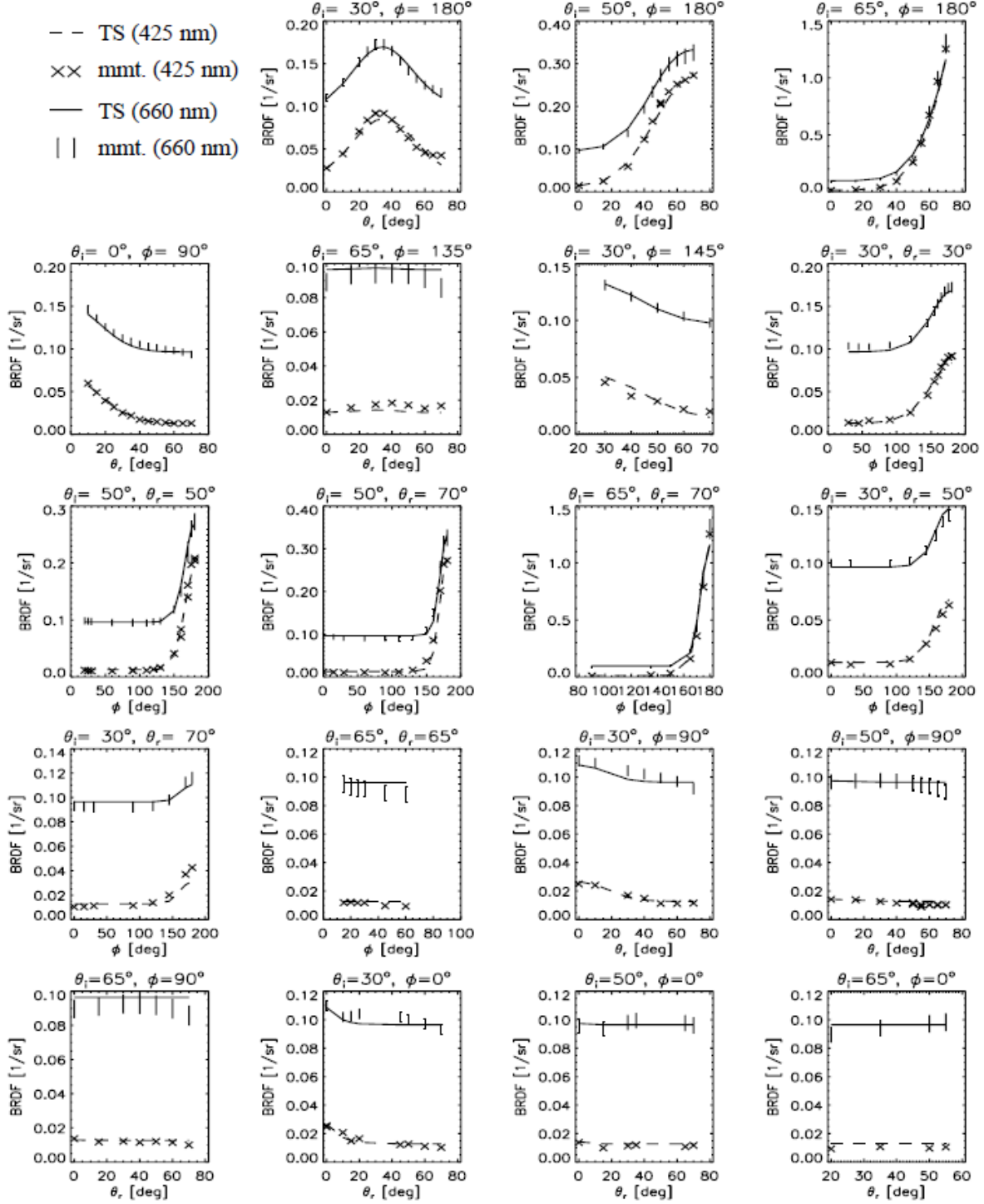


Figure 4.7: Red concrete: mixed reflectance model (Lambertian + TS) fitting to measured BRDF

with a total system weight of approximately 9kg. It allows for measuring the spectral BRDF over a 140-degree range (-70° - 70°) to within 3 degrees of backscatter. These measured BRDF data were fitted using Hapke's SHOE model described in Section (3.8) wherein a series expansion of

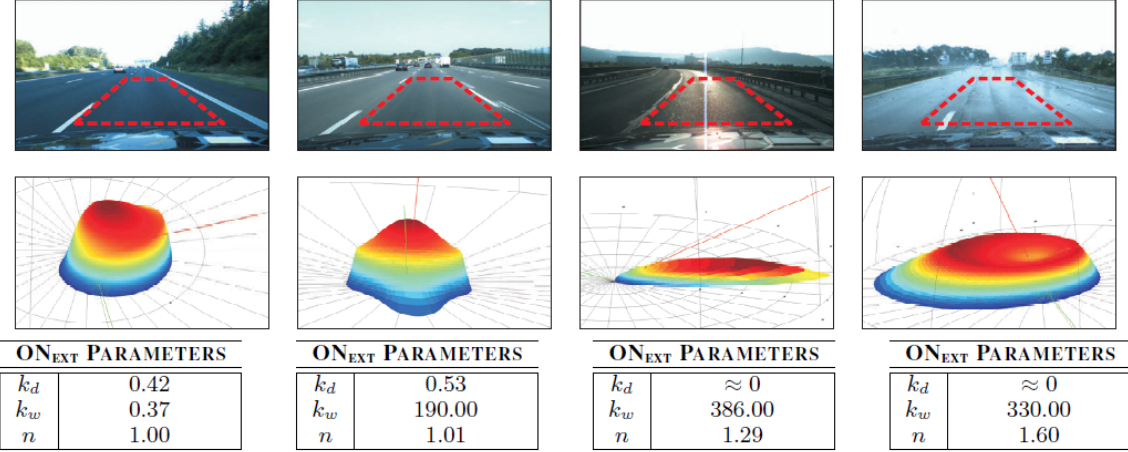


Figure 4.8: Concrete road: mixed reflectance model (ON + TS) fitting to measured BRDF

Legendre Polynomials was substituted for the angularly dependent backscatter function. The best-fit model BRDF was then integrated over the hemisphere to compute the Directional Hemispheric Reflectance (DHR), as shown in Fig 4.9. It can be observed that the integrated Lab BRDF (black) is almost overlapped with the measured DHR (blue), verifying the effectiveness of this BRDF model in capturing reflectivities of beach sands.

Apart from the beach sands, many spectral reflectance measurements on 13 different igneous rocks (seen in Fig.4.10) and their powders with different sizes in visible and near-infrared range from 400nm to 2500nm were performed by Zhuang et al. [35]. Similar to the experimental set-up in [34], the spectrometer and the light source were mounted on manually operated goniometer that consists of two rotary stages with bars, as shown in Fig 4.1(d). This set-up design is capable of adjusting the viewing and the incident zenith angles from 0° to 70° continuously. To emit the spectrum from 400nm to 2500nm, the light source they utilized was highly stable Newport 66502-250Q-R1 quartz tungsten halogen lamp with an adjustable power range from 0-250W. The reflected light is collected by a bare fiber and transmitted to Spectral Evolution SR-2500 spectrometer. In their work, they measured respectively the intensities from the target sample and the reference Lab-sphere Spectralon plaque at incident zenith angle of 0° and a viewing zenith of 30°. Their ratio was considered as the relative reflectance, which is used to compute the reflectance factor (REFF) of this sample by multiplying the absolute Spectralon REFF values measured by RELAB [35]. These measurements were then fitted also using the Hapke's SHOE model, where the phase function is

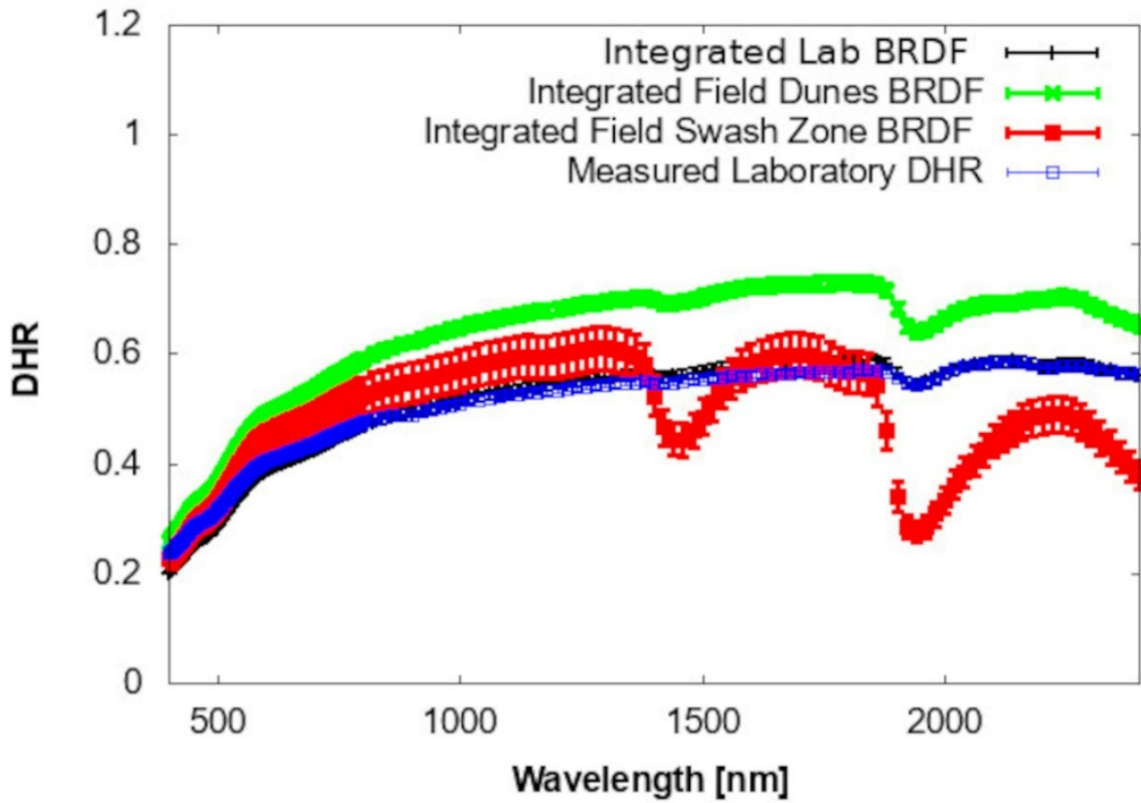


Figure 4.9: Chincoteague Island beach sand: Hapke's SHOE model fitting to measured DHR

approximated by an empirical two-term Legendre polynomial. As illustrated in Fig 4.11, the fitted spectral reflectance curves for some samples with particle sizes exceeding $675\mu m$ are too similar to be clearly distinguished. It can also be observed that this model may not produce accurate spectral reflectance for all samples and particle sizes, likely due to its inherent simplicity and the assumption of a constant refractive index ($n = 1.6$) irrespective of wavelengths.

Alongside studies on road materials, the optical properties of road markings have attracted increasing attention in recent years. Spieringhs et al. [32] carried out several experiments on three different types of road markings (seen in Fig 4.12) using a Large Near-Field Goniometer (LNFG) developed by TechnoTeam, as shown in Fig.4.1(b). The elements highlighted in blue, red, and green boxes correspond to the luminance camera, the fixed light source, and the sample holder, respectively. In their measurements, a TechnoTeam LMK 98-4 high-tech calibrated luminance camera with a resolution of 1390×1040 pixels was mounted in the RIGO801 LNFG, which can be moved freely in order to allow for measurements in all desired viewing angles. Then the camera

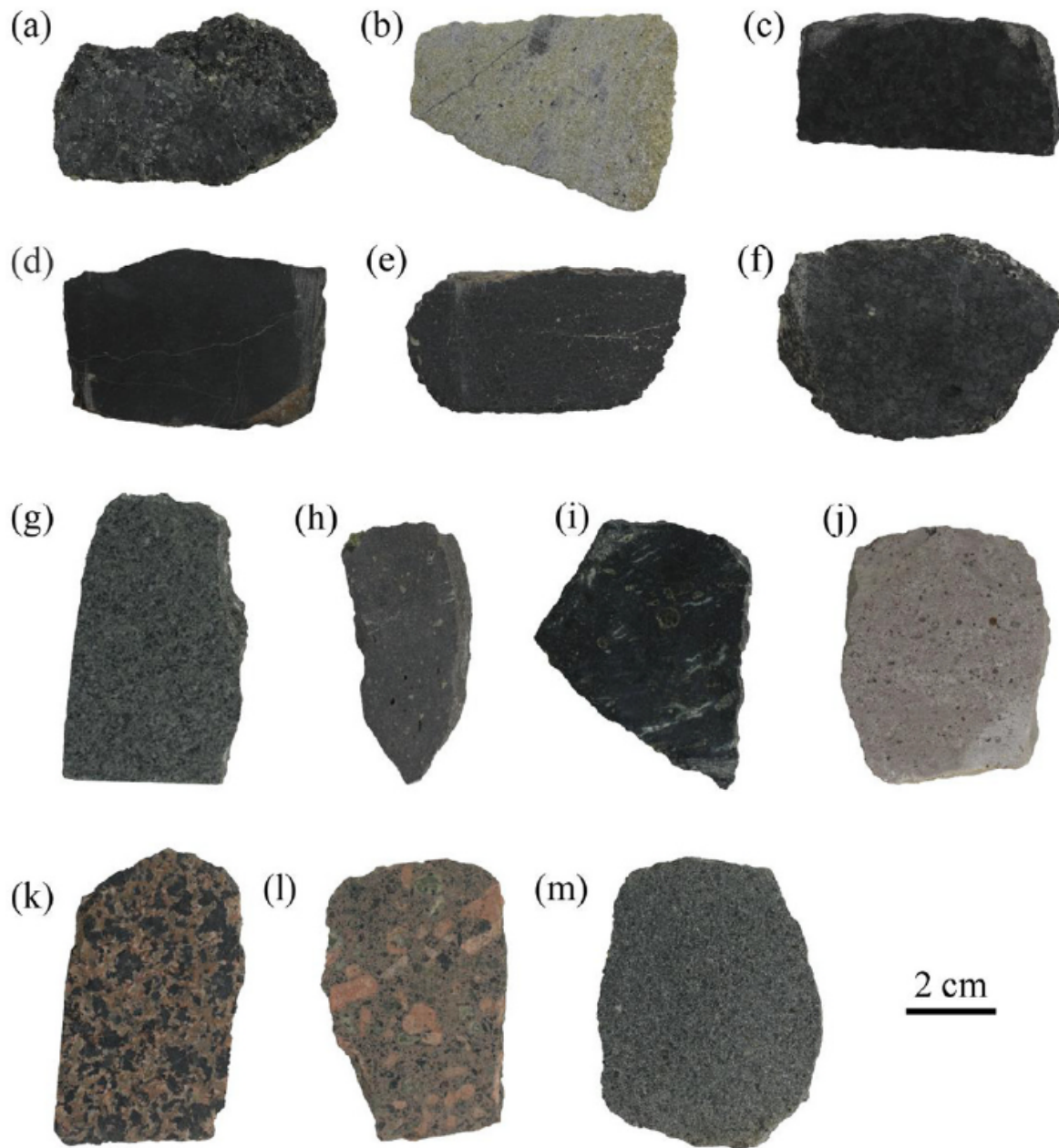


Figure 4.10: 13 igneous rocks slabs with a thickness of 1.5 cm: (a) Dunite; (b) Peridotite; (c) Olivine pyroxenolite; (d) Picrite porphyrite; (e) Kimberlite; (f) Gabbro; (g) Diabase; (h) Olivine basalt; (i) Andesite basalt; (j) Trachyte; (k) Pyroxenite syenite; (l) Orthophyre; (m) Lamprophyre.

and the RIGO801 LNFG are connected to the computer in order to set the position of the arm of the LNFG via the TechnoTeam software and to record the luminance images. A QTH10(/M) Quartz Tungsten-Halogen 50W 12V lamp with a broadband emission between 400 and 2200nm

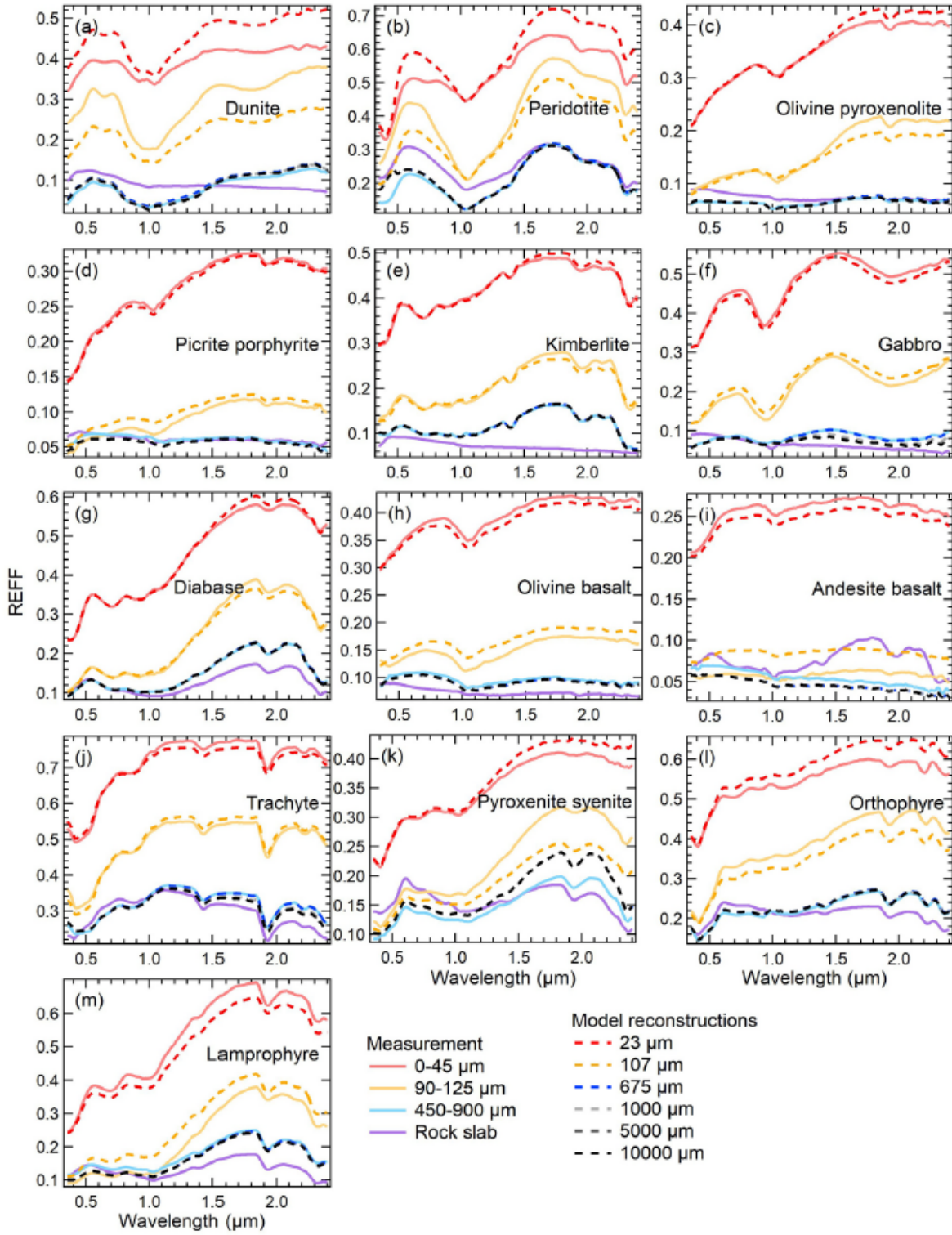


Figure 4.11: Igneous rocks: Hapke's SHOE model fitting to measured REFF

was employed as light source and connected to programmable Delta Elektronika SM1500 DC power system. Notice that the position of light source is fixed, indicating that it is impossible to allow



Figure 4.12: Three road marking samples containing glass beads: (1) SWARCO Limboplast *D*480 with Megalux 0.6 – 1.5 KT14, (2) SWARCO Limboplast *D*480 with *P*21 3 : 1, and (3) 3MStamark *A*650.

for all desired incident angles (θ, φ) by changing the position of light source. To accommodate this, an adjustable sample holder was designed to enable rotation around both vertical and horizontal axes. These measured data for 3 road markings were shown in Fig 4.13. As the incident angle θ_i increases, retro-reflection and specular reflection become more pronounced. Particularly at $\theta_i = 80^\circ$, the BRDF in the retro-direction nearly reaches or exceeds 1. To able to predict the BRDF at any incident angles (θ_i, φ_i) and viewing angles (θ_r, φ_r) , the authors employed the retro-phong model (described in Section (3.7)) to fit the measurements. A fitting example for road marking sample 1 was presented in Fig .4.14. Compared to the other models evaluated in [32], this model demonstrated better fitting performance.

4.2 Solar Albedo Measurements of Road Materials

4.2.1 Albedo Measurement set-up

Similar to BRDF measurements, there exist two primary approaches of measuring solar albedo: laboratory-based and field-based measurements. [16]. The former is carried out indoors using a

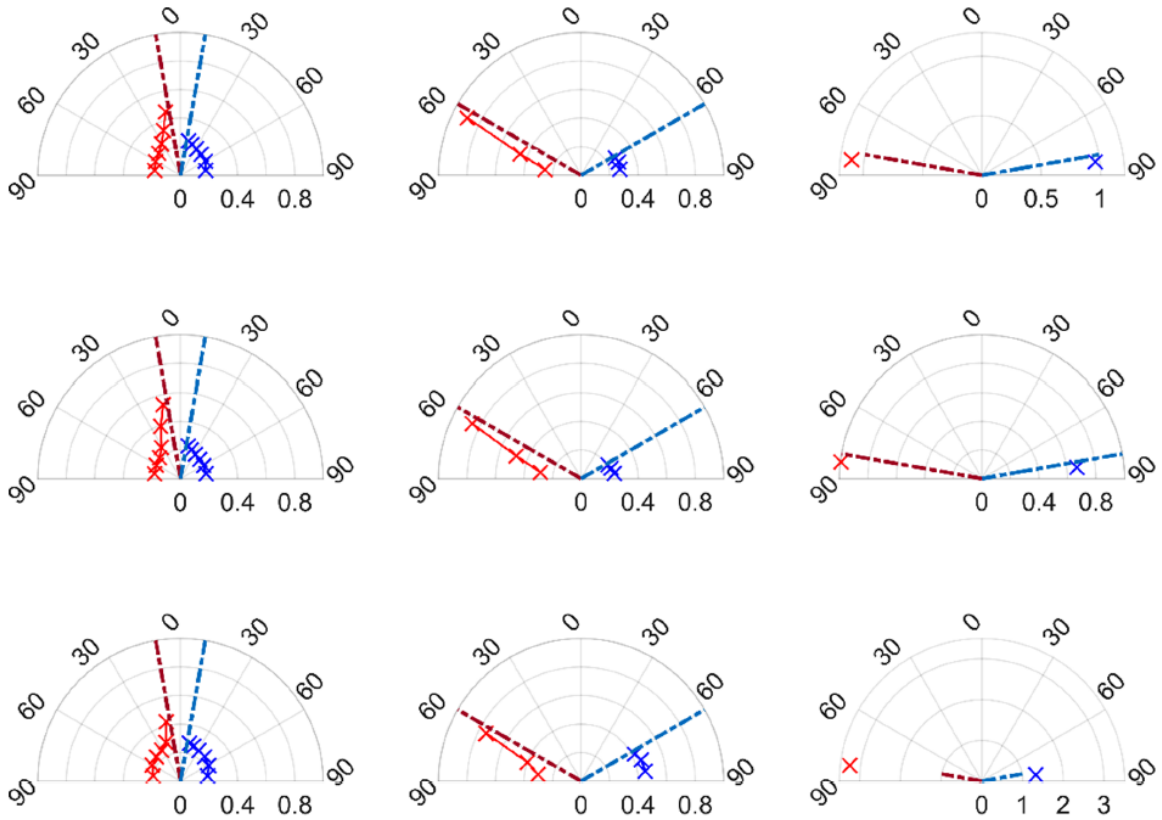


Figure 4.13: Measured BRDF: Top row for sample 1, middle row for sample 2, bottom row for sample 3. The 3 plots in a row represent an incident angle of $\theta_i = 0^\circ, 60^\circ, 80^\circ$ for a fixed φ_i from left to right, respectively. The crosses and dashed lines in red represent the retro-reflective hemisphere, and the ones in blue represent the specular hemisphere. The red dotted lines indicate the incident vectors. The radius of the polar diagrams is in sr° .

spectrophotometer equipped with integrating spheres, as following the standard test ASTM E903. The goal is to obtain the spectral reflectance which is an approximate estimate of solar albedo. This kind of test method is applicable to materials having both specular and diffuse optical properties.

While the latter is following ASTM 1918, providing a realistic measure of solar albedo, but highly depending on the weather conditions. It is conducted outside using an albedometer composing of sky-facing and target-facing pyranometers parallel to the test surface, as seen Fig 4.15, which are used to measure the incoming and reflected solar radiation respectively. The two pyranometers are mounted on an arm and a stand that centers the sensor at a height of 500mm above the target surface in order to minimize the effects of sensor, arm, and stand shadows on measured

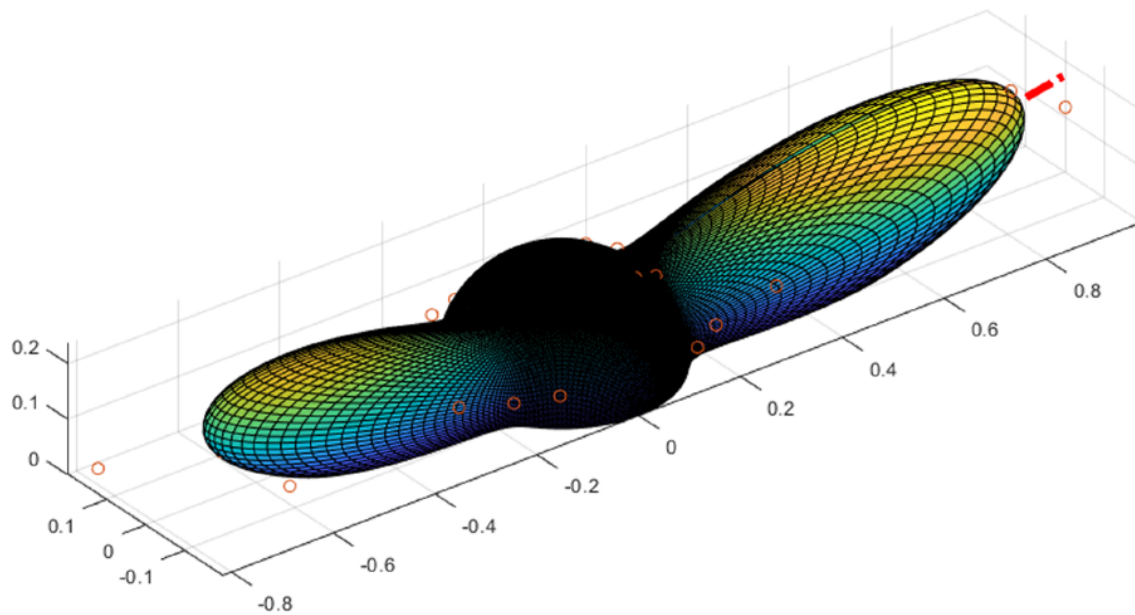


Figure 4.14: Road marking sample 1 (SWARCO Limboplast D480 withMegalux 0.6 – 1.5 KT14): Retro-Phong model fitting to measured BRDF. The dashed lines indicate the incident direction, the colored grids represent the fitted BRDF, the dots indicate the measured BRDFs in different viewing angles

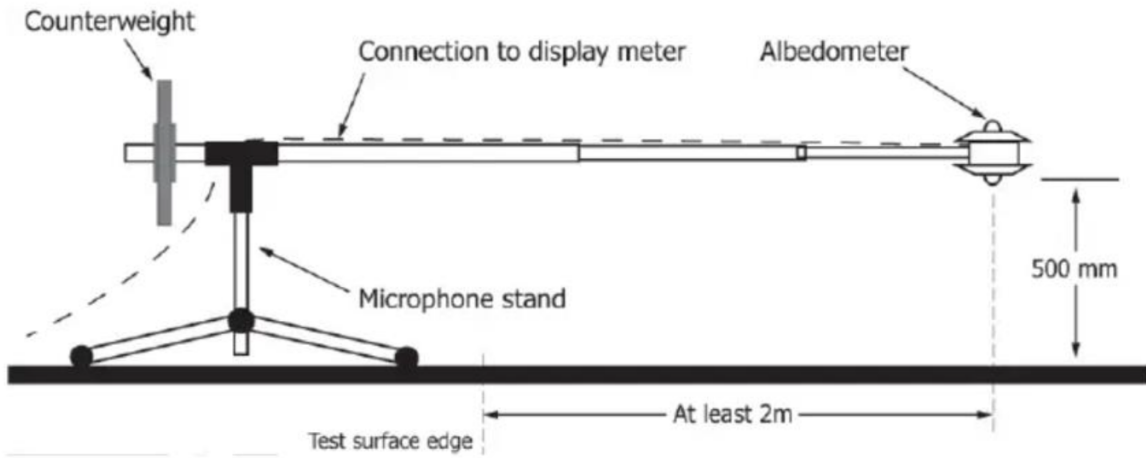


Figure 4.15: Schematic of the Albedometer and Its Support (provided in ASTM 1918-21)

reflected radiation. The horizontal distance from the center of the pyranometer to the edge of the test surface has to be at least 2m. Besides, the arm and stand should be strong and cast the smallest possible shadow. This test method applies to low-sloped surface which are at least 4m in diameter (if circular) or at least 4m on each side (if rectangular). Notice that the angle of the

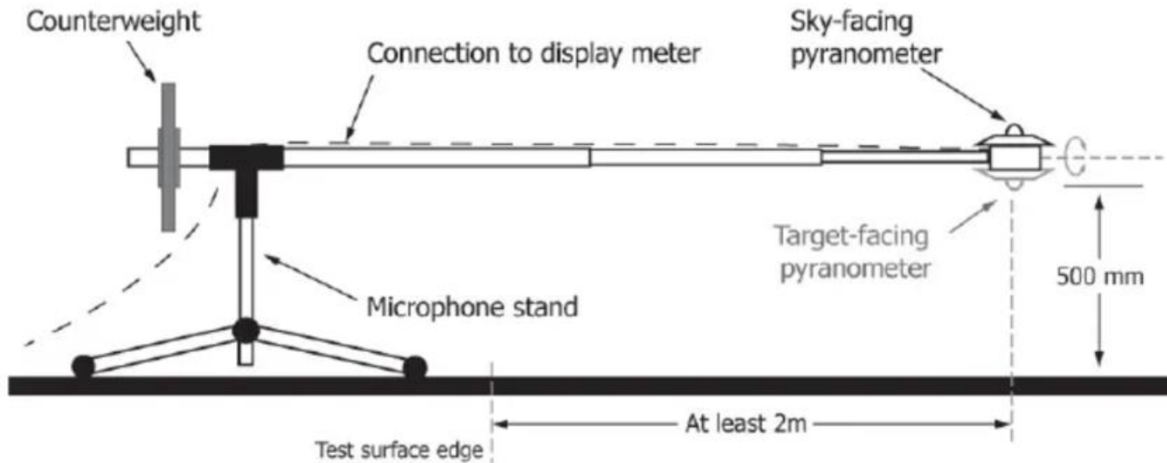


Figure 4.16: Schematic of the Pyranometer and Its Support (provided in ASTM 1918-21)

sun to the normal of the test surface should be less than 45° . Due to horizontal and low-sloped surfaces, the hours in summer for this test should be between 9.a.m and 3.p.m local standard time, which is when solar radiation is at least 70% of the value obtained at noon for that day. In winter, conducting the test should be between 10.a.m and 2.p.m local time, considering low solar incident angle. The albedometer will read both the incoming solar radiation and the reflected solar radiation simultaneously. To ensure the accuracy, each reading should be constant for at least 10s before recording the its values. Plus, at least 3 pairs of incoming and reflected radiation are required to be measured within 2 minutes. The calculated solar reflectance which is the ratio of the reflected radiation to the incoming radiation need to agree to within 0.01 in a reflectivity scale of 0 to 1.

The field-based method can be also conducted using only a pyranometer, as illustrated in Fig 4.16. Initially, the pyranometer is positioned facing upward and parallel to the test surface to measure the incoming solar radiation. After this measurement, the device is flipped to face downward to capture the reflected radiation. This reading process is quite similar to that of an albedometer. However, there is a key distinction due to time delay between reading incoming and reflected radiation. Unlike the albedometer, it requires at least three pairs of measurements of incoming and reflected radiation taken within a span of 10 minutes to ensure accuracy and reliability in the results for this one-pyranometer set-up.

4.2.2 Previous Work on Solar Albedo Measurements of Road Materials

Over the past few decades, many researchers performed the solar albedo measurements on road materials, in order to understand their ability to reflect solar radiation. Different from BRDF measurements, the measurements of solar albedo offers a practical and integrated assessment of surface reflectivity over the whole hemisphere. In the 1980's, Blumthaler et al. investigated the solar albedo of some road materials (e.g., asphalt, rock, stream sand, and limestone) over the $0.3 - 3\mu m$ wavelength range [36], as summarized in Table 4.1. These values were obtained through many measurements carried out using a star-pyranometer under both direct sunlight and cloudy conditions, with no essential differences observed between the two cases. At each measurement site, the albedo value was determined as the mean of five individual readings. The measured albedo values varied considerably among the materials, with asphalt exhibiting the lowest albedo (0.06-0.15, average 0.10) and limestone the highest (0.20-0.32, average 0.26).

Table 4.1: Solar albedo of various road materials

Road Materials	Number of sites of Measurements	Solar albedo		
		Min	Max	Mean
Asphalt	12	0.06	0.15	0.106
Primitive rock	7	0.12	0.16	0.144
Stream sand	8	0.22	0.24	0.238
Stream sand	15	0.20	0.32	0.260

Later, Kushari et al. utilized two coupled-pyranometers (LP PYRA 05 made by Hotek Technologies, seen in Fig 4.17) to conducted field measurements on road sections in Bangkok Metropolitan's district [7], in order to gather albedo data from $0.3 - 3\mu m$ wavelength range. This dual-faced sensor (also known as albedometer) was able to capture the incoming and reflected solar radiation in the same time, which were then read through a multi channel data logger (from Campbell Scientific), as illustrated in Fig .4.17. Each reading last for a period of 1 to 2 minutes. All these measurements were performed under direct sunlight in clear day from 10am to 4pm. A total of 149 measurement

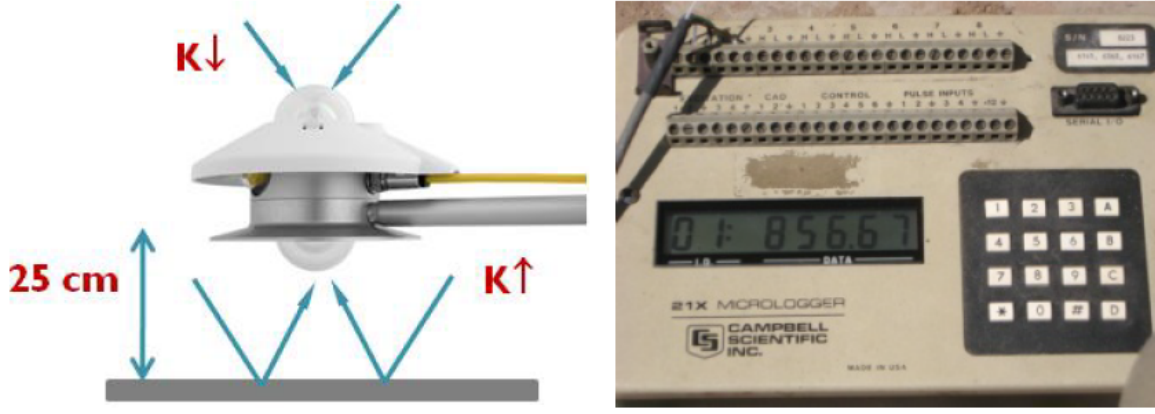


Figure 4.17: Two coupled-pyranometers (left) and a multi channel data logger

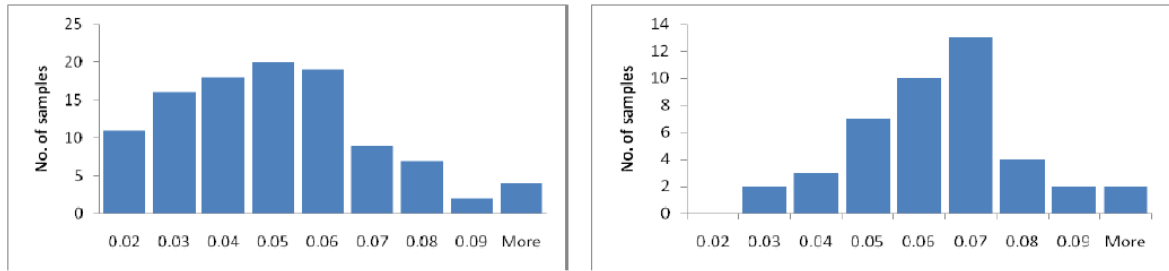


Figure 4.18: Albedo distribution of 106 asphalt samples (left) and 43 concrete samples (right)

points were selected, including 106 samples from asphalt pavements and 43 from concrete pavements. The collected albedo data for the types of pavements are summarized in Fig .4.18, showing that both asphalt and concrete exhibit low albedo values. The mean albedo of the former is 0.045, substantially lower than the value reported in [36] (0.106). In comparison, the latter demonstrated a higher mean albedo of 0.061.

A similar albedometer [16] was adapted for the laboratory measurements shown in Fig.4.19, focusing on three asphalt mixtures (Fig.4.20) and three portland cement concrete (Fig 4.21) with different roughness level in the same wavelength range. In this experimental set-up, the solar radiation was emitted from the infrared lamp with wavelength of $0.3 - 3\mu m$. Unlike the field measurements in [7], data for incident and reflected radiation were not collected simultaneously. The lamp and the albedometer were first positioned at the same height above the samples, in order to measure reflected radiation from the lower pyranometer every 30 seconds over a period of 3 minutes. The final recorded reflected is the mean value of these readings. Then the albedometer



Figure 4.19: Albedo lab-based measurement set-up

was moved to the position of the sample, and the incident radiation from upper pyranometer was collected. The asphalt mixture samples were made of crushed basalt aggregate, limestone filler, and modified asphalt, while the Portland cement concrete was made of aggregate, cement, and sand. Their measured albedo are summarized in Fig.4.22. We can clearly observe that the later mixture (albedo from 0.228 to 0.264) has higher reflectance than the former (albedo 0.0546 to 0.0611). Moreover, the albedo values of the asphalt mixture are consistent with those published in [7, 36], providing a reliable reference for future investigations.

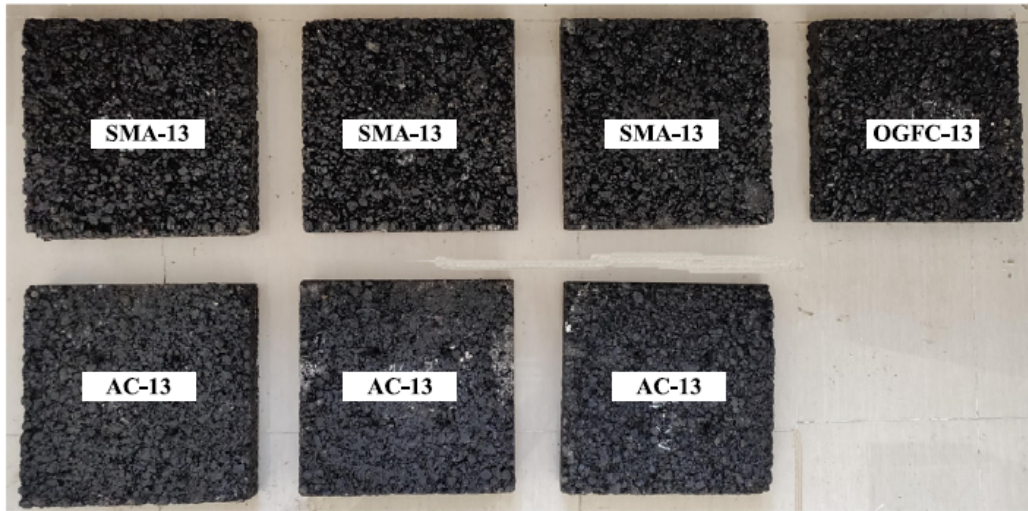


Figure 4.20: 3 types of asphalt mixtures

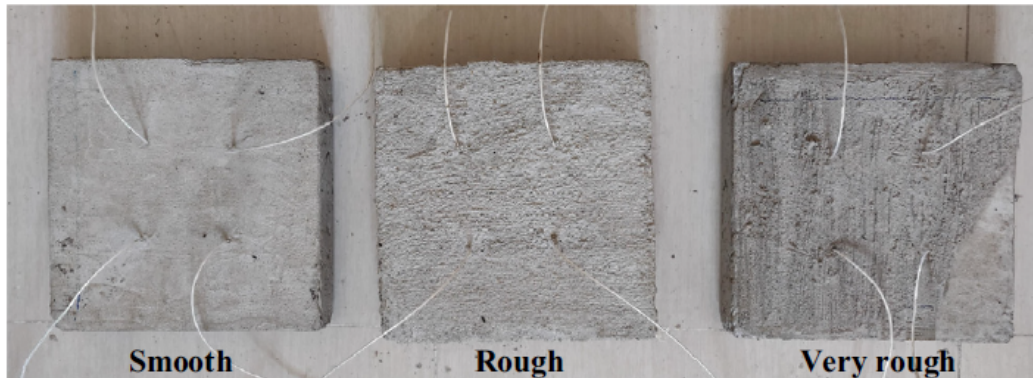


Figure 4.21: portland cement concrete (PCC)

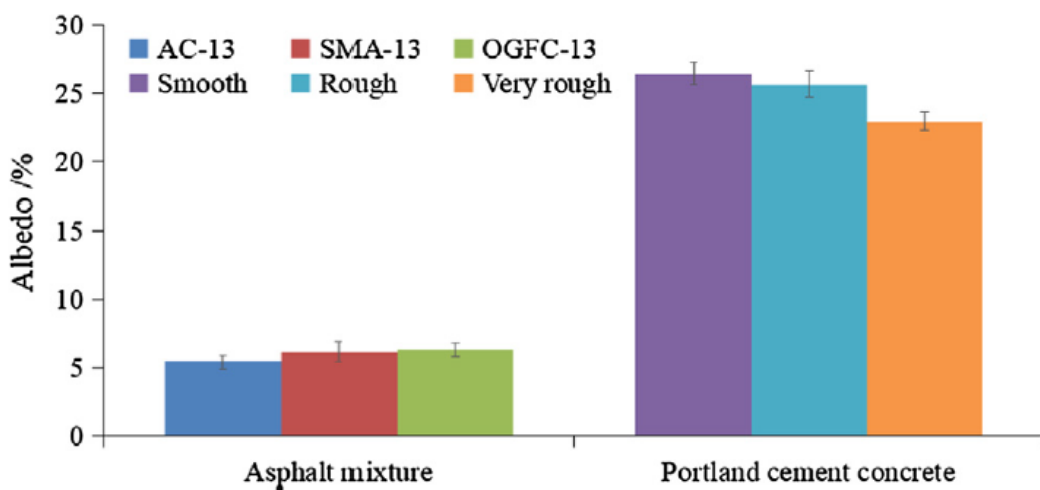


Figure 4.22: Albedo of asphalt mixtures and PCC without coating materials

Chapter 5

Spectral BRDF Measurement of road samples

The design and operation of a transport system require careful consideration of numerous things, such as the installation of public lighting, minimizing light pollution, temperature control, and ensuring the visibility of road markings. Central to addressing these considerations is to know the reflectance of the road surface, which necessitates simulations or measurements. However, conducting these simulations or measurements is often costly due to the time requirements and the need for specialized equipment. A key question arises: Can the reflectance of a road surface be predicted if the formulation of the surface and the reflectance of its individual components are known? The relationship between solar albedo and BRDF provides a pathway to answering this question. Equations (2.18) and (2.17) illustrate how solar albedo can be derived from BRDF. This indicates that if the BRDF model can predict the BRDF for any given direction of incidence and observation, then it can also predict the solar albedo of the surface. Chapter 3 provides several BRDF models expressed as functions of incident and viewing angles. However, these models often require additional parameters that depend on the surface's characteristics. For instance, the ON model requires knowledge of the diffuse albedo (ρ) and surface roughness (σ). For each single-material component, we can calibrate a reflectance model by fitting it to spectral BRDF measurements and extracting the relevant parameters. Once BRDF models are established for

each individual component, they can be combined to construct a hybrid BRDF model for the multi-material pavement. This model can then be fitted to the BRDF measurements to determine the weighting factors associated with each component. Accordingly, the BRDF of this pavement can be predicted for any direction of incidence and observation. However, achieving this lies in obtaining accurate and reliable spectral BRDF measurements, which serve as essential input to the fitting process.

To support this, this chapter first introduces 4 formulations of road samples and their constituent components. Then it provides a spectral BRDF measurement method using the equipments developed by Cerema to measure their BRDF. This approach is validated first through comparison with results obtained from Université Gustave Eiffel (UGE), and then through BRDF measurements on Spectralon (a material with well-known Lambertian reflection model and a given diffuse albedo). The measured spectral BRDF results for both the composite (mix-material) and individual (single-material) samples are presented and analyzed in the last section.

5.1 Road samples

This section first presents 4 different formulations of road samples, along with their individual constituent materials, as provided by a French company. In order to ensure reliable BRDF measurements for each single-component sample, it is required that the surface to be measured must be flat. For this purpose, this section then describes how to construct such samples.

5.1.1 4 Formulations

The 4 formulations of road samples (F1, F2, F3, and F4) and their respective components are illustrated in Figure 5.1, with their component proportions summarized in Table 5.1. Each formulation incorporates limestone filler, a very fine powder present in small proportions. As such, the impact of limestone filler has been disregarded in the analysis. Formulations F1 and F4 share similar component structures, as do F2 and F3. The primary distinction between F1 and F4 lies in the aggregate composition: F1 incorporates a single type of rock, whereas F4 includes a mixture of two different rock types. Meanwhile, the difference between F2 and F3 is in the binder: F2

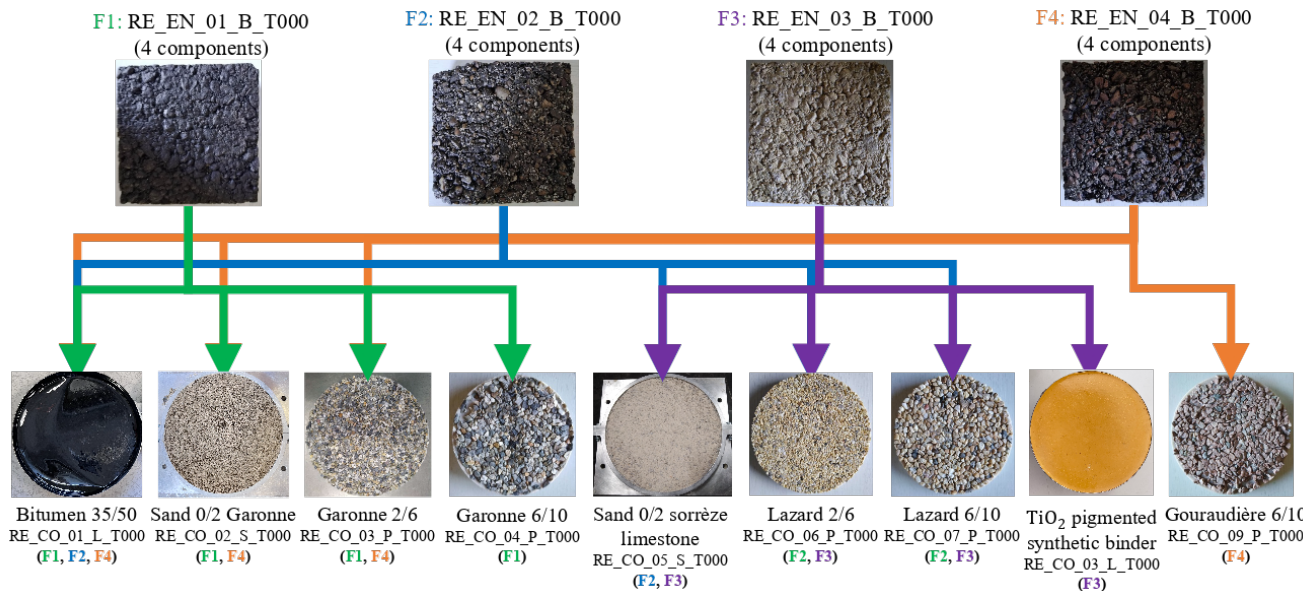


Figure 5.1: 4 formulations of roads and their components

uses bitumen, while F3 employs a pigmented synthetic binder TiO_2 . Across all single-component samples, the materials can be broadly classified into two categories: binders and aggregates. The binders include bitumen and the synthetic binder. The aggregates comprise four main types:

- Garonne rock in three size fractions (0/2 mm, 2/6 mm, and 6/10 mm),
- Sorrèze limestone (0/2 mm),
- Lazard rock in two size fractions (2/6 mm and 6/10 mm),
- Gouraudière rock (6/10 mm).

5.1.2 Construction of single-material samples

The procedure for fabricating a one-component sample with a flat surface is as follows:

1. Prepare all the materials and tools including:

- 3 liquid products (as illuminated in Fig 5.2): Renlease QZ511, REN HY956 from Ren-Shape and Resin - RENLAM MS-1
- Aluminum mould, as seen in Fig 5.3(a)

Table 5.1: 4 formulations

	F1	F2	F3	F4
Limestone filler	1.4%	2.2%	1.4%	1.9%
TiO_2	/	/	0.5%	/
Bitumen	5.2%	5.3%	/	5.4%
Synthetic binder	/	/	5.4%	/
Garonne (0/2)	31.1%	/	/	29.5%
Garonne (2/6)	19.2%	/	/	19.8%
Garonne (6/10)	43.1%	/	/	/
Sorèze limestone (0/2)	/	28.3%	27.5%	/
Lazard (2/6)	/	19.5%	21%	/
Lazard (6/10)	/	44.7%	44.2%	/
Gouraudière (6/10)	/	/	/	43.4%
Total	100%	100%	100%	100%

- Brush
 - Stainless steel spatula
 - Mixing container
 - Clean aggregates
 - Fontainebleau sands
2. Clean the mould, then install the aluminum mould and secure it with 2 screws.
 3. Coating the mould with unmold liquid Renlease QZ511 using the brush, as seen in Fig 5.3(b).
 4. Put a single layer of aggregates, making sure they are as close together as possible, as seen in Fig 5.4(a).
 5. Place a layer of sand on top of the aggregate to prevent the resin from passing through the pores between the aggregates, as shown in Fig 5.4(b).

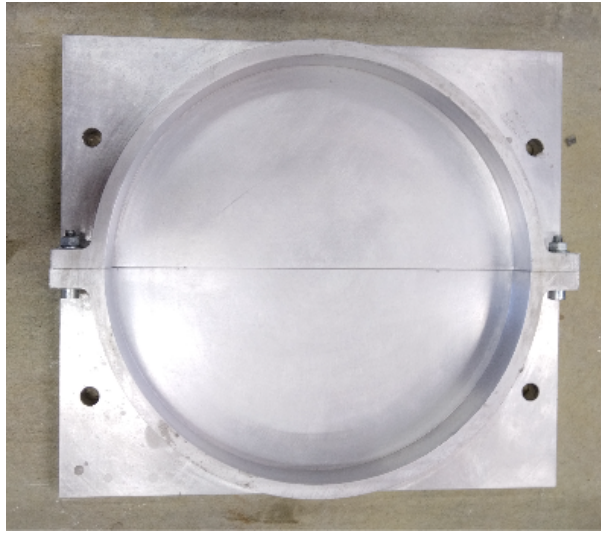


Figure 5.2: 3 liquid products: Unmould liquid - Renrelease QZ511 (left), Hardener - REN HY956 from RenShape (middle), Resin - RENLAM MS-1 (right)

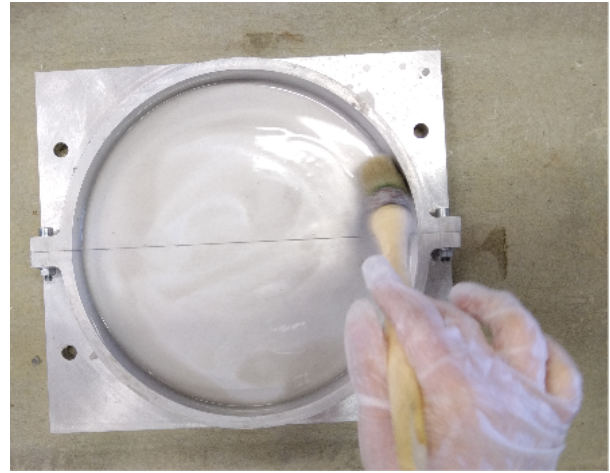
6. Put 300g of RENLAM MS-1 resin and 100g of REN HY956 hardener in the mixing container, and mix them together, then put in 800g of Fontainebleau sand, as seen in Fig 5.5(a).
7. Mix the sands with the liquids in the container until homogenous, then leave them (see Fig 5.5(b)) for about 1 hour to warm up.
8. Pour the homogenous glue into the mould until it is full, then make sure the top surface is flat and leave to rest for 8 hours, as seen in Fig 5.6(a)
9. Unmould this mould and remove the sand from the surface of the aggregates, as shown in Fig 5.6(b).

5.2 Spectral BRDF Measurement

This section describes a measurement set-up developed by Cerema (see in Fig. 5.7), allowing for the elimination of environmental interferences and ensuring precise control over experimental conditions.

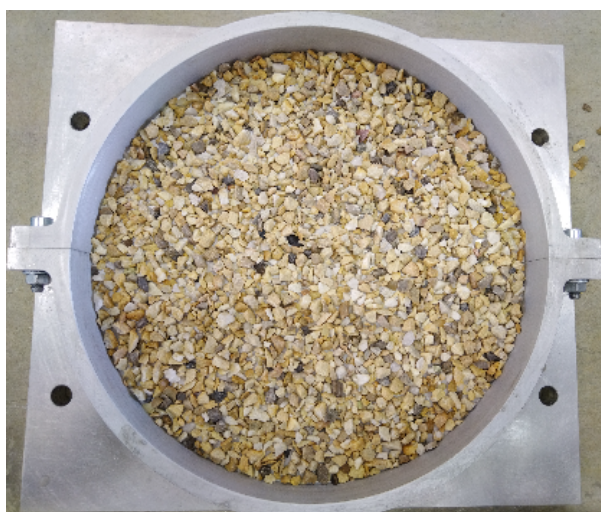


(a) Clean aluminum mould

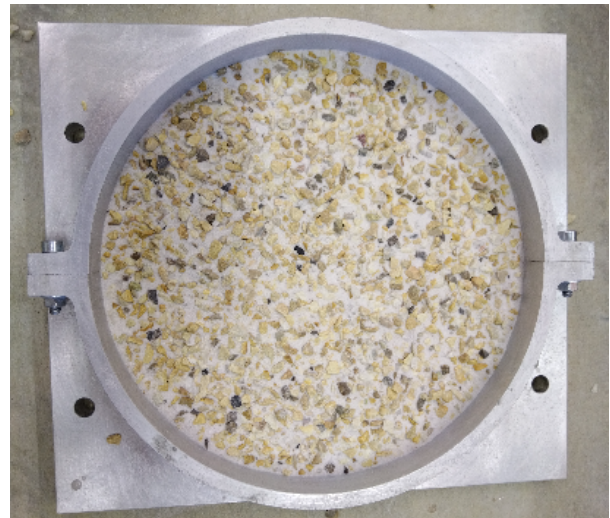


(b) Coating aluminum mould

Figure 5.3: Aluminum mould



(a) Put a single layer of aggregates on the mould



(b) Put a single layer of sands on the aggregates

Figure 5.4: Placing the aggregates on the mould

5.2.1 Spectral BRDF Measurement set-up: the Gonioreflectometer at Cerema

The Gonioreflectometer is composed of:

- light source: Halogene lamp (350nm -2500nm)
- reception sensor: spectroradiometer

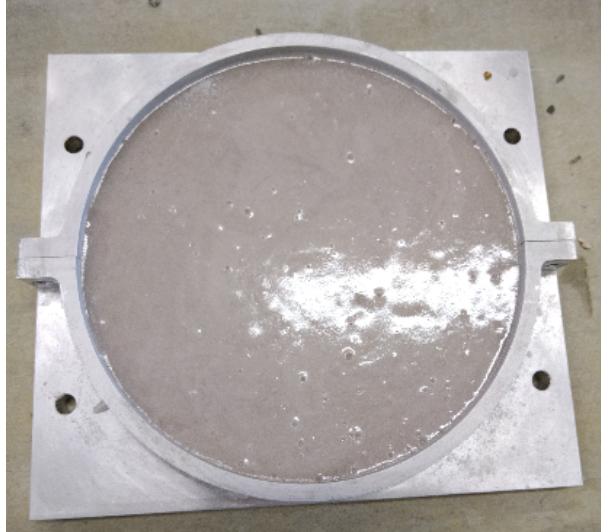


(a) Put all materials in the container



(b) Homogenous glue after mixing

Figure 5.5: Making the glue



(a) Pour the glue on the mould



(b) Final sample

Figure 5.6: Unmold

- goniometer: changing the incident angle and viewing angles

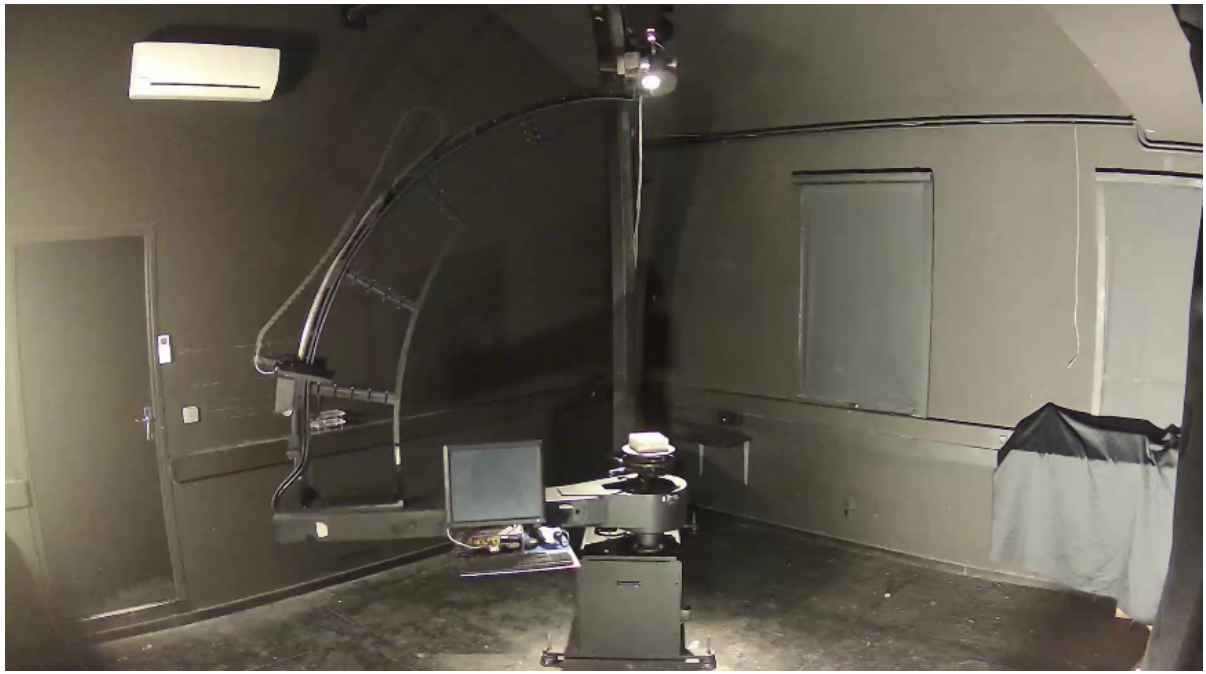


Figure 5.7: Gonioreflectometer (Cerema)

5.2.2 Measurement steps

- step 1 - installation of the spectroradiometer

There are several spectroradiometers: 1° and 5°

- step 2 - installation of the sample
- step 3 - launch the software (GonioPilotageDesAxes) to turn on the Halogene lamp

When the software is on, then in this software

1. set the parameters
 - choose COM3
 - choose where to save the result files
2. turn on COM ESP301 (green means it is on)
3. turn on the lamp (green means it is on)
4. access the measured screen

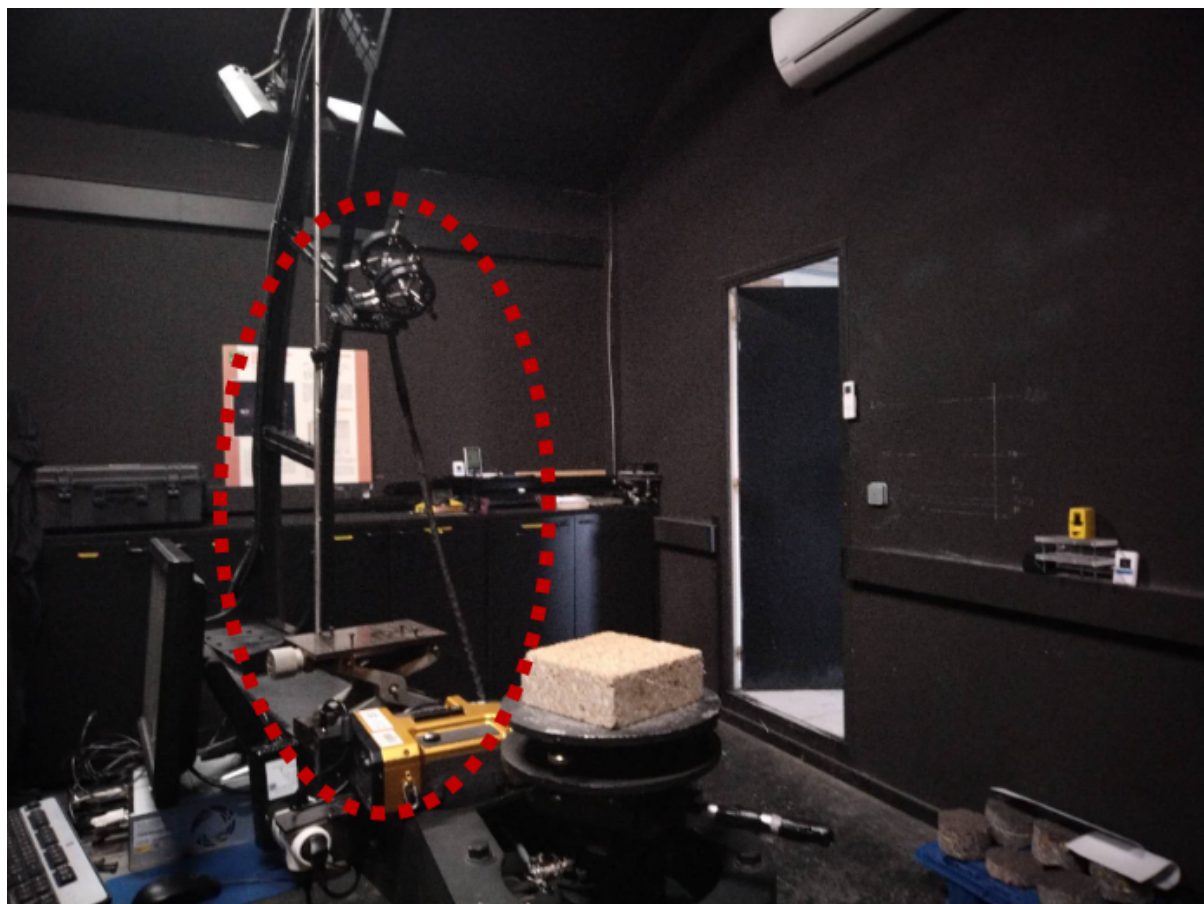


Figure 5.8: Gonio-spectroradiometer (Cerema)

5. activate the remote control (yellow mean it is on)
- step 4 - launch python code to start the measurement
 1. modify the α , and change the saving sql file name for corresponding α
 2. change the height of spectroradiometer
 3. launch the spectral evolution
 4. launch the python codes
 5. once the python codes is done, stop the spectral evolution
- step 6 - send sql file and measured radiance to Sebastian and receive the results in .csv file

Measurement set-up:

Provide the diagram of measurement set-up.

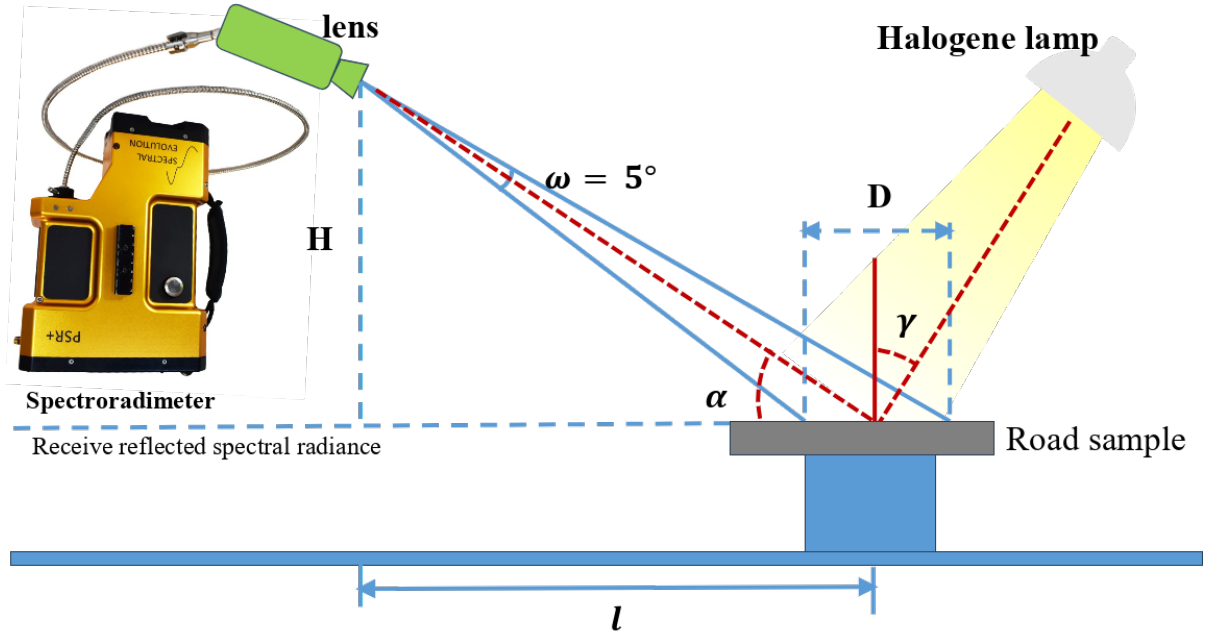


Figure 5.9: Gonio-spectroradiometer (Cerema)

5.2.3 Comparison with UGE

First we compared our results with that of UGE, to see if our measured matched with that of UGE. For most configurations, there is a good match, but for some configurations, like large incident. For these cases, there are direct light reaching the lens, leading to more radiance detected by the spectroradiometer. To further validate our method, we measure the BRDF of Spectralon which offers Lambertian BRDF with given diffuse albedo.

5.2.4 Validation with Spectralon

So here we will provide the BRDF along the wavelength ($350nm - 2500nm$) and its BRDF distribution which should be unit hemisphere.

5.3 Results

5.3.1 Methodology

The wavelength $350nm$ to $2500nm$

Measurement scenario

- l - the horizontal distance between the sample and the spectroradiometer
- H - the height difference between spectroradiometer and the sample
- γ - the incident angle ($\gamma = \theta_i$): $0^\circ - 90^\circ$
- α - the observation angle ($\alpha = \frac{\pi}{2} - \theta_r$): $0^\circ - 90^\circ$
- β - the angle between the vertical planes of illumination and observation ($\beta = \pi - (\phi_r - \phi_i)$)
- δ - the angle between the observation plane and the roadway (x) axis ($\delta = \phi_r - \pi$)

5.3.2 Results of 4 Mixed Road-Material Samples

Figure : in the same figures, plot 4 curves respectively for F1, F2, F3, F4 For a given configuration $(\theta_i, \phi_i, \theta_r, \phi_r)$: the BRDF along the wavelength (350nm – 2500nm)

Analyze Figure 1:

- comparison between F1 and F4: 1 rock different
- comparison between F2 and F3: the binder different

Figure: BRDF distribution: 2 subfigures respectively for F1 and F4

Figure: BRDF distribution: 2 subfigures respectively for F1 and F4

Figure: For given $(\theta_i, \phi_i, \theta_r)$: plot 4 curves in polar system Analyze Figure 4:

- comparison between F1 and F4: 1 rock different
- comparison between F2 and F3: the binder different

5.3.3 Results of 3 Mastics

Mastic 1 for F1 and F4: bitume and rock Garonne

Mastic 2 for F2: bitume and rock calcaire sorrèze

Mastic 3 for F3: Liant de synthèse pigmenté TiO2 and rock calcaire sorrèze

mastic 1 vs mastic 2: the rock different

mastic 2 vs mastic 3: the binder different

Figure: in the same figures, plot 4 curves respectively for F1, F2, F3, F4 For a given configuration $(\theta_i, \phi_i, \theta_r, \phi_r)$: the BRDF along the wavelength (350nm – 2500nm)

Analyze Figure:

- comparison between F1 and F4: 1 rock different
- comparison between F2 and F3: the binder different

Figure: BRDF distribution: 2 subfigures respectively for F1 and F4

Figure: BRDF distribution: 2 subfigures respectively for F1 and F4

Figure: For given $(\theta_i, \phi_i, \theta_r)$: plot 4 curves in polar system Analyze Figure 4:

- comparison between F1 and F4: 1 rock different
- comparison between F2 and F3: the binder different

5.3.4 Results of Single Road-Material Samples

5.3.4.1 Lazard

different size of lazard

- Lazard 2/6
- Lazard 6/10

Figure: in the same figures, plot 4 curves respectively for 2 different size rocks For a given configuration $(\theta_i, \phi_i, \theta_r, \phi_r)$: the BRDF along the wavelength (350nm – 2500nm)

Figure: BRDF distribution: 2 subfigures respectively for 2/6 and 6/10

Figure: For given $(\theta_i, \phi_i, \theta_r)$: plot 2 curves in polar system

5.3.4.2 Garonne

different size of Garonne

- Garonne 2/6
- Garonne 6/10

Figure: in the same figures, plot 4 curves respectively for 2 different size rocks For a given configuration $(\theta_i, \phi_i, \theta_r, \phi_r)$: the BRDF along the wavelength (350nm – 2500nm)

Figure: BRDF distribution: 2 subfigures respectively for 2/6 and 6/10

Figure: For given $(\theta_i, \phi_i, \theta_r)$: plot 2 curves in polar system

5.3.4.3 Gouraudière

Figure: in the same figures, plot 3 curves respectively for the same size rocks For a given configuration $(\theta_i, \phi_i, \theta_r, \phi_r)$: the BRDF along the wavelength (350nm – 2500nm)

Figure: BRDF distribution: for Gouraudière Comparing to Lazard and Garonne

Figure: For given $(\theta_i, \phi_i, \theta_r)$: plot 3 curves in polar system for the same size rocks

Chapter 6

Modelling of road samples

6.1 Modelling of Single Road-Material Samples and Materials

6.1.1 Methodology

introduce the fitting methods: gradient descent, levenberg-Marquardt etc

Introduce the BRDF models used to fit the measurement

6.1.2 BRDF Fitting to Measurements

6.1.2.1 BRDF Fitting: Lazard

6.1.2.2 BRDF Fitting: Garonne

6.1.2.3 BRDF Fitting: Gouraudière

6.1.2.4 Fitting Results of 3 Mastics

6.2 Modelling of 4 Mixed Road-Material Samples

6.2.1 Existing methods of Mixing BRDF

This section presents the methods to mix the BRDF, linear or non-linear combination of two or more BRDFs

6.2.2 BRDF Construction of F1

6.2.3 BRDF Construction of F2

6.2.4 BRDF Construction of F3

6.2.5 BRDF Construction of F4

Chapter 7

Conclusion and Perspectives

7.1 Conclusion

7.2 Perspectives

Bibliography

- [1] Valérie Muzet, Sébastien Liandrat, Vincent Bour, Jérôme Dehon, and Jean-Pierre Christory. Is it possible to achieve quality lighting without considering the photometry of the pavements? In *Conference CIE 2021, NC Malaysia*, pages 11–25, 2021.
- [2] Valérie Muzet, Florian Greffier, Aurélia Nicolaï, Alexandre Taron, and Paul Verny. Evaluation of the performance of an optimized road surface/lighting combination. *Lighting Research & Technology*, 51(4):576–591, 2019.
- [3] Giuseppe Rossi, Paola Iacomussi, and Michele Zinzi. Lighting implications of urban mitigation strategies through cool pavements: energy savings and visual comfort. *Climate*, 6(2):26, 2018.
- [4] Tomasz E Burghardt, Harald Mosböck, Anton Pashkevich, and Mario Fiolić. Horizontal road markings for human and machine vision. *Transportation research procedia*, 48:3622–3633, 2020.
- [5] Wojciech Jarosz. *Efficient Monte Carlo methods for light transport in scattering media*. University of California, San Diego, 2008.
- [6] Martin Roser and Philip Lenz. Camera-based bidirectional reflectance measurement for road surface reflectivity classification. In *2010 IEEE Intelligent Vehicles Symposium*, pages 340–347. IEEE, 2010.
- [7] Berlian KUSHARI and Kunawee KANITPONG. Surface albedo of bangkok roads. In *Proceedings of the Eastern Asia Society for Transportation Studies Vol. 8 (The 9th International Conference of Eastern Asia Society for Transportation Studies, 2011)*, pages 181–181. Eastern Asia Society for Transportation Studies, 2011.

- [8] Mathieu Hébert. *Optical models for material appearance*. EDP Sciences Les Ulis, France, 2022.
- [9] Fred E Nicodemus. Directional reflectance and emissivity of an opaque surface. *Applied optics*, 4(7):767–775, 1965.
- [10] Rosana Montes and Carlos Ureña. An overview of brdf models. *University of Grenada, Technical Report LSI-2012-001*, 2012.
- [11] István Lazányi and László Szirmay-Kalos. Fresnel term approximations for metals. *Winter School of Computer Graphics (WSCG), Short papers*, 2(6), 2005.
- [12] Christophe Schlick. An inexpensive brdf model for physically-based rendering. In *Computer graphics forum*, volume 13, pages 233–246. Wiley Online Library, 1994.
- [13] Zander Majercik. The schlick fresnel approximation. In *Ray Tracing Gems II: Next Generation Real-Time Rendering with DXR, Vulkan, and OptiX*, pages 109–114. Springer, 2021.
- [14] Jiří Filip. Analyzing and predicting anisotropic effects of brdfs. In *Proceedings of the ACM SIGGRAPH Symposium on Applied Perception*, pages 25–32, 2015.
- [15] Ying Qu, Shunlin Liang, Qiang Liu, Tao He, Suhong Liu, and Xiaowen Li. Mapping surface broadband albedo from satellite observations: A review of literatures on algorithms and products. *Remote Sensing*, 7(1):990–1020, 2015.
- [16] Jun Chen, Zheng Zhou, Jiantao Wu, Shuguang Hou, and Mengcheng Liu. Field and laboratory measurement of albedo and heat transfer for pavement materials. *Construction and Building Materials*, 202:46–57, 2019.
- [17] Paola Iacomussi, Giuseppe Rossi, et al. Influence of material characterization in the design of tunnel lighting installations. In *CIE Washington 2019*, pages 546–552. 2019.
- [18] Eric Heitz. Understanding the masking-shadowing function in microfacet-based brdfs. *Journal of Computer Graphics Techniques*, 3(2):32–91, 2014.
- [19] Michael Oren and Shree K Nayar. Generalization of the lambertian model and implications for machine vision. *International Journal of Computer Vision*, 14:227–251, 1995.

- [20] Gerhard Meister. *Bidirectional reflectance of urban surfaces*. PhD thesis, Staats-und Universitätsbibliothek Hamburg Carl von Ossietzky, 2000.
- [21] Simon Lucas, Mickaël Ribardière, Romain Pacanowski, and Pascal Barla. A micrograin bsdf model for the rendering of porous layers. In *SIGGRAPH Asia 2023 Conference Papers*, pages 1–10, 2023.
- [22] Simon Lucas, Mickaël Ribardière, Romain Pacanowski, and Pascal Barla. A fully-correlated anisotropic micrograin bsdf model. *ACM Transactions on Graphics*, 43(4):111, 2024.
- [23] Bruce Walter, Stephen R Marschner, Hongsong Li, and Kenneth E Torrance. Microfacet models for refraction through rough surfaces. *Rendering techniques*, 2007:18th, 2007.
- [24] Kenneth E Torrance and Ephraim M Sparrow. Theory for off-specular reflection from roughened surfaces. *Journal of the Optical society of America*, 57(9):1105–1114, 1967.
- [25] Robert L Cook and Kenneth E. Torrance. A reflectance model for computer graphics. *ACM Transactions on Graphics (ToG)*, 1(1):7–24, 1982.
- [26] Michael Ashikhmin and Peter Shirley. An anisotropic phong brdf model. *Journal of graphics tools*, 5(2):25–32, 2000.
- [27] Lionel Simonot. Photometric model of diffuse surfaces described as a distribution of interfaced lambertian facets. *Applied optics*, 48(30):5793–5801, 2009.
- [28] Csaba Kelemen and Laszlo Szirmay-Kalos. A microfacet based coupled specular-matte brdf model with importance sampling. In *Eurographics (short presentations)*, 2001.
- [29] Brent Burley and Walt Disney Animation Studios. Physically-based shading at disney. In *Acm siggraph*, volume 2012, pages 1–7. vol. 2012, 2012.
- [30] Eric PF Lafourture, Sing-Choong Foo, Kenneth E Torrance, and Donald P Greenberg. Non-linear approximation of reflectance functions. In *Proceedings of the 24th annual conference on Computer graphics and interactive techniques*, pages 117–126, 1997.

- [31] Nicolas Gimonet, Aurélien Cord, and Guillaume Saint Pierre. How to predict real road state from vehicle embedded camera? In *2015 IEEE Intelligent Vehicles Symposium (IV)*, pages 593–598. IEEE, 2015.
- [32] Rik Marco Spieringhs, Jan Audenaert, Kevin Smet, Ingrid Heynderickx, and Peter Hanselaer. Road marking brdf model applicable for a wide range of incident illumination conditions. *JOSA A*, 40(3):590–601, 2023.
- [33] Bruce Hapke. Bidirectional reflectance spectroscopy. *Icarus*, 59(1):41–59, 1984.
- [34] John E Wise and John C Mars. Field reflectance measurements at night of beach and desert sands within a particulate brdf model. *Remote Sensing*, 14(19):5020, 2022.
- [35] Yan Zhuang, Hao Zhang, Pei Ma, Te Jiang, Yazhou Yang, Ralph E Milliken, and Weibiao Hsu. Visible and near-infrared reflectance spectra of igneous rocks and their powders. *Icarus*, 391:115346, 2023.
- [36] M Blumthaler and W Ambach. Solar uvb-albedo of various surfaces. *Photochemistry and photobiology*, 48(1):85–88, 1988.
- [37] Ruiqiang Bai, Mingyi Zhang, Jiwei Wang, Guanji Li, and Zhilang You. Study on the solar albedo characteristics of pavement and embankment slope surfaces in permafrost regions. *Solar Energy*, 237:352–364, 2022.